2017

Plasma Dynamics of Laser Filaments

Danielle Reyes
University of Central Florida

PLASMA DYNAMICS OF LASER FILAMENTS

by

DANIELLE L. REYES
B.S. University of Central Florida, 2015

A thesis submitted in partial fulfillment of the requirements
for the degree of Master of Science
in the Department of Physics
in the College of Sciences
at the University of Central Florida
Orlando, Florida

Spring Term
2017

ABSTRACT

Laser filamentation is a complex phenomenon occurring for pulses with peak power above a critical value. A filament is a dynamic self-guided structure characterized by several unique qualities, which include a beam with a high-intensity core surrounded by an energy reservoir, a weakly ionized plasma channel, and supercontinuum generation. Several of the proposed applications for filamentation utilize the plasma channel, such as for assisted electric discharge and microwave guiding. However, filament properties are highly influenced by the physical conditions under which they are formed. A host of studies have been conducted to further characterize filaments, but much work still remains in order to understand their complex behavior. This work presents an accurate and direct measurement of the electron density based on an interferometric technique. The impact of different initial parameters on filament spatio-temporal dynamics in air is investigated, concentrating primarily on their influence on the plasma. For comparison of the experiment with theory, the plasma decay is modeled by a system of kinetic equations that takes into account three-body and dissociative electron recombination reactions.

ACKNOWLEDGMENTS

I would like to acknowledge, first and foremost, my advisor, Dr. Martin Richardson, for providing me with the opportunity to perform research as a member of LPL. It has been an excellent experience working with the members of LPL and being exposed to the many types of research going on in this group.

I would also like to acknowledge the other committee members, Dr. Michael Chini and Dr. Romain Gaume, for their time, guidance, and input.

I am very grateful for Dr. Shermineh Rostami-Fairchild and Dr. Matthieu Baudelet. Their encouragement, counsel, and guidance has been invaluable throughout this entire process. Though they are very busy individuals, they always make time for my many questions and are ready to hear of my triumphs or troubles in the lab and advise me accordingly.

I would like also like to acknowledge the other members of the filamentation team with whom I have worked in the past: Dr. Magali Durand, Dr. Khan Lim, Dr. Nicholas Barbieri, Dr. Cheonha Jeon, Daniel Kepler, Jesse Ethan Lane, Daniel Thul, Haley Kerrigan, and Teodor Malendovych. I am thankful for their friendship and support throughout my time here. I owe a special thanks to Magali, Khan, and Cheon for their pivotal role in familiarizing me with the lab and preparing me to perform experiments on my own as an undergraduate student. I would also like to thank Ethan, Dan, Haley, and Teo for either staying with me or helping me in the lab while preparing for and collecting the data presented in this thesis.

The laser development team within LPL, particularly Dr. Lawrence Shah, Nathan Bodnar, and Joshua Bradford, have spent countless hours either refitting or upgrading the MTFL laser facility used for this research, for which I am very grateful.

Though it would be impossible to list them all here, my research experience thus far would not have been nearly as beneficial without the support and encouragement of my friends, colleagues, and classmates. However two that deserve special mention are Jasmine Thompson and Kelley Flinn.

Finally, my family has been incredibly encouraging and supportive throughout this process. My parents in particular have poured many years of their lives into raising me to be the person that I am today. I constantly point to my father as the one who first inspired me to pursue science and my mother as the one who gives me the love of puzzle-solving and determination necessary to conduct research. I would like to dedicate this research to them. I would be remiss to not mention my faith in Jesus Christ and the support of my church family during this time. Last but not least, my husband, Justin Reyes, has been a constant source of reassurance and inspiration. Without him and his commitment to walk this road beside me, this work would not be possible.

TABLE OF CONTENTS

LIST OF FIGURES

LIST OF TABLES

LIST OF ACRONYMS

AOPDF	acousto-optic programmable dispersive filter
CCD	charge-coupled device
CCN	cloud condensation nuclei
FIBS	femtosecond laser induced breakdown spectroscopy
FWHM	full-width at half-maximum
GVD	group velocity dispersion
LIDAR	light detection and ranging
MPI	multi-photon ionization
MTFL	Multi-Terawatt Femtosecond/Filamentation Laser
NA	numerical aperture
NLSE	nonlinear Schrodinger equation

CHAPTER 1 – INTRODUCTION

1.1 – Filament Formation

1.1.1 – Kerr Effect and Self-focusing

The total refractive index of a propagation medium includes an intensity dependent term,

$$n = n_0 + n_2 I \quad (1)$$

where n_0 is the linear refractive index and I is the optical intensity. The nonlinear refractive index, n_2, is related to the third order susceptibility. At high intensities, $n_2 I$ becomes significant, causing an increase in the total refractive index. This intensity dependent change in the refractive index is called the Kerr effect. The resulting nonlinear phase shift is often expressed as the B-integral [1]:

$$B = k_0 \int_0^z n_2 I dz \quad (2)$$

A B-integral having a value as high as π is considered significant. Since the intensity of the beam is highest at the center and tapers off towards the edges, the change in refractive index encountered by the beam, which is proportional to the intensity, will likewise be highest on axis, resulting in a lensing effect (Figure 1a). For example, for a beam with a Gaussian intensity profile, Δn will have a Gaussian profile as well, and the resulting approximate phase shift, when expanded, can be shown to resemble that due to a parabolic lens. Thus the Kerr effect leads to self-focusing of the beam.

The characteristic length for self-focusing, L_{SF}, is defined as the length over which the B-integral changes by a factor of one [1].

$$L_{SF} = \frac{1}{n_2 k_0 I_0} \quad (3)$$

where n_2 is the nonlinear refractive index, k_0 is the wavenumber for the central laser wavelength, and I_0 is the peak intensity.

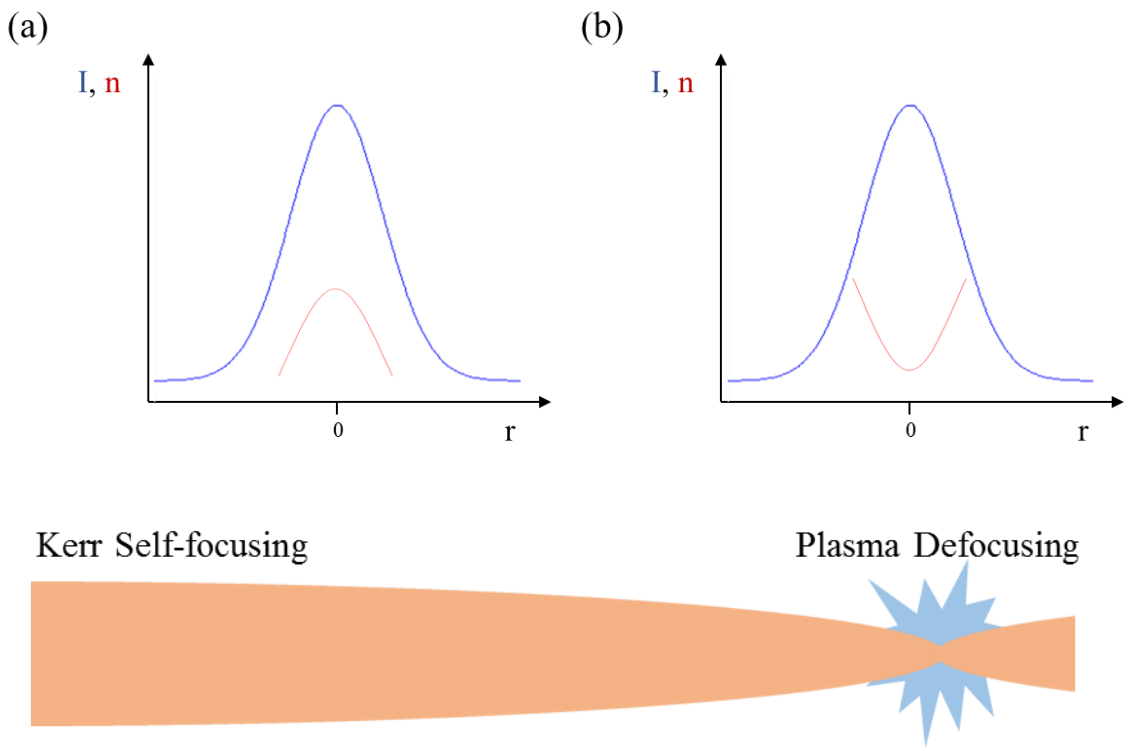

Figure 1: Illustration depicting (a) the Kerr effect, in which the change in refractive index is proportional to the intensity profile causing the beam to self-focus, and (b) plasma defocusing, in which the negative phase shift induced by the presence of plasma acts as a negative lens.

Collapse of the beam, or the onset of self-focusing, occurs when the initial peak power of the beam is greater than the critical peak power. At this power, self-focusing effects overcome diffractive effects. The following equation for P_{cr} is valid for a Gaussian beam [1]:

$$P_{cr} = 3.77\lambda_0^2/8\pi n_0 n_2 \qquad (4)$$

where λ_0 is central laser wavelength and n_0 and n_2 are the linear and nonlinear refractive indices respectively. The factor of 3.77 is valid for a Gaussian beam and will vary based on the beam shape. For a Gaussian beam with $\lambda_0 = 800$ nm in air, $P_{cr} \approx 3.2\ GW$. Other beam profiles will have different critical powers. The length which a Gaussian beam will propagate until collapse, L_c, is given by the Marburger equation [2].

$$L_c = \frac{0.367 L_{DF}}{\sqrt{\left[(P_{in}/P_{cr})^{\frac{1}{2}} - 0.852\right]^2 - 0.0219}} \quad (5)$$

where L_{DF} is the Rayleigh length. This semi-empirical formula fails at high input powers (~$100P_{cr}$). A transition occurs from $1/\sqrt{P_{in}}$ to $1/P_{in}$ at higher powers.

1.1.2 – Photo-ionization and Plasma-defocusing

For a filament to form, the photon energy must be much less than the ionization potential of the propagation medium. If not, the pulse will gradually attenuate due to two or three photon absorption [1]. As the light intensity increases, the probability of multiphoton ionization and tunneling ionization increases. Multiphoton ionization (MPI) arises when an electron simultaneously absorbs enough photons to overcome the ionization potential, U_i, a phenomena that can be described by perturbation theory (Figure 2a). The rate of MPI scales as I^K, where K is the number of photons absorbed concurrently [3]. Tunneling ionization results when an electron tunnels through the potential barrier due to both the electric field of the laser and the Coulomb potential of the nucleus (Figure 2b). Tunneling ionization requires a higher intensity than MPI. They are collectively referred to as photo-ionization.

The Keldysh parameter, γ, delineates the dominant mechanism of photoionization.

$$\gamma = \frac{\omega}{e}\sqrt{\frac{m_e U_i n_0 c \varepsilon_0}{I}} \quad (6)$$

where ω is the laser frequency, e is the electron charge, m_e is the mass of an electron, U_i is the ionization potential, n_0 is the linear refractive index, c is the speed of light, ε_0 is the permittivity of free space, and I is the optical intensity. If $\gamma \gg 1$, MPI is the prevalent mechanism, but if $\gamma \ll 1$, tunneling ionization prevails.

Air largely consists of oxygen and nitrogen, the lower ionization potential belonging to oxygen (12 eV). For a laser with photon energies of $\hbar\omega \approx 1.55$ eV (at 800 nm), ionization will not result from the absorption of a single photon. In order for the laser to induce ionization, an electron would have to simultaneously absorb 8 photons. That is, $K \sim 8$ in air. Therefore a high number of photons in a minute quantity of space and time, and thus high intensity, is required in order for the ionization to become probable. Sufficient intensity is achieved as the beam begins to self-focus.

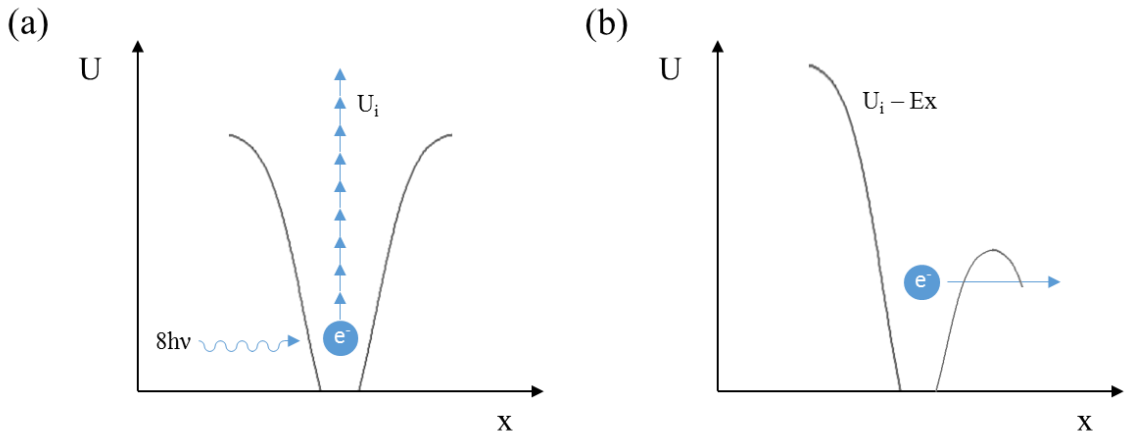

Figure 2: Diagram illustrating (a) multiphoton ionization and (b) tunneling ionization.

Free electrons due to photo-ionization can be accelerated in the electric field of the trailing end of the pulse due to inverse Bremsstrahlung. This refers to the phenomena in which the electron collides with the nucleus and gets jolted out of phase from the E-field, and thus the oscillatory energy of the electron is converted to kinetic energy. The resulting energetic electrons produce further ionization due to collisions with neighboring atoms in a process referred to as avalanche ionization.

Plasma generation due to photo-ionization reduces the local refractive index. The resulting change in n (the derivation is shown in section 2.3.1), is given by the following,

$$\Delta n \approx -\frac{\rho}{2\rho_c} \quad (7)$$

where $\rho_c = \varepsilon_0 m_e \left(\frac{2\pi c}{e\lambda_0}\right)^2$ is the critical plasma density, at which point the plasma becomes opaque ($\rho_c \approx 1.7 \times 10^{21}$ cm^{-3} for $\lambda_0 = 800$ nm). The quantities ε_0, m_e, e, c, and λ_0 are respectively the permittivity of free space, electron mass, electron charge, speed of light, and central laser wavelength. The presence of plasma results in a local refractive index change that is lowest on axis and increases towards the edges of the pulse, resembling the shape of a negative lens. Thus the plasma causes defocusing of the beam (Figure 1b). The characteristic length of plasma defocusing, L_{PL}, is defined as the length over which the B-integral due to the plasma (Eq. 8) deviates by a factor of one (Eq. 9) [1],

$$B = -k_0 \int_0^z \frac{\rho}{2n_0\rho_c} dz \quad (8)$$

$$L_{PL} = \frac{2n_0\rho_c}{k_0\rho_{at}} \quad (9)$$

where ρ_{at} is the neutral atom density. For $\rho_{at} = 2 \times 10^{19}$ cm^{-3} and an electron density of $\rho = 10^{16}$ cm^{-3}, $L_{PL} \approx 22\ \mu m$. The length scale for defocusing is given by $L_{PL}\rho_{at}/\rho$. Multiphoton absorption attenuates the beam. The length scale for multiphoton absorption, L_{MPA}, is the length over which the pulse is attenuated by a factor of $[(K+1)/2]^{1/(K-1)}$ [1].

$$L_{MPA} = \frac{1}{2K\hbar\omega_0\sigma_K I^{K-1}\rho_{at}} \quad (10)$$

where σ_K is the ionization cross-section and K is the number of photons simultaneously absorbed. For $\lambda_0 = 800\,nm$ in air ($K = 8$ and $\sigma_8 = 3.7 \times 10^{-96}$ $cm^{16}W^{-8}s^{-1}$) and $I = 5 \times 10^{13}$ W/cm^2, $L_{MPA} \approx 12.6$ m.

Once the initial self-focusing of the beam occurs, a dynamic balance is achieved between these competing self-focusing and defocusing effects, until the arrest of collapse. The dynamic spatial replenishment model [4] describes how the focusing-defocusing cycle produces a beam with a high-intensity core (~100 μm in diameter), surrounded by an energy reservoir, maintained for distances greater than the Rayleigh length, leaving a plasma channel in its wake. Though it may seem that arrest of collapse results from plasma defocusing, other factors such as higher order nonlinearity, nonlocal effects, nonlinear absorption, and, in solids, the GVD, all may factor in to arrest collapse.

1.2 – Properties of Filaments

1.2.1 – Plasma and Intensity Clamping

In regions of plasma formation, further self-focusing is locally limited due to the defocusing effect of the plasma. When these two intensity dependent processes, the Kerr effect and plasma defocusing, achieve a balance, the peak intensity is said to be clamped inside the filament [5]. Likewise, the peak plasma density is clamped, as the probability of further ionization is intensity dependent. The clamping intensity can be approximated by equating the Δn due to the Kerr effect and plasma [5].

1.2.2 – Supercontinuum Generation

Ionization, self-steepening, and self-phase modulation all contribute to spectral broadening during filamentation [1]. The temporal variation of the refractive index results in an instantaneous

frequency that is related to the time derivative of I and proportional to the propagation distance z. The ensuing self-phase modulation generates redder frequencies at the leading edge of the pulse and bluer frequencies at the trailing edge. The intensity dependence of the refractive index causes the peak of the pulse to travel at a slower velocity than the trailing edge, leading to a steepening of the pulse. Pulse self-steeping generates bluer light at the tail of the pulse. Finally, ionization contributes bluer frequencies on the trailing edge of the pulse.

1.2.3 – THz Radiation

The free electrons in the electric field of the pulse experience a ponderomotive force, accelerating them towards the weak field direction. As a result, some of the electrons in the plasma will travel faster than the velocity of the light in the propagation medium leading to Cherenkov-like emission of THz [6].

1.3 – Applications of Filamentation

One potential application is to use the filament plasma channel to guide lightning. During lightning formation, the initial process is leader formation, in which a weakly ionized plasma channel descends from the cloud. As the electric field on the earth's surface increases, the air becomes conductive and breaks down to form a corona discharge. Once the channel is formed, the electrons flow through the channel to neutralize the cloud. Filaments have been demonstrated to initiate corona discharge in clouds [7, 8]. Therefore, filaments can be used to induce lightning. The plasma channel of the filament would also provide a path of least resistance through which the cloud could discharge, thereby guiding the lightning.

Another possibility is to use filamentation as a remote THz source. THz radiation has several advantages over other light sources for spectroscopy [6]. The radiation is safe to biological

tissue and provides decent resolution. In addition, many materials can be uniquely identified by their spectrum in the THz regime, including explosive materials. Unlike other THz sources, which will diffract and be absorbed by water in the air at great distances, filaments have the promising ability to deliver THz radiation for spectroscopy at long distances.

In addition, by forming a cylindrical sheath of filaments with a hollow core, the structure could act as a waveguide for microwave radiation [9, 10]. The lower refractive index of the plasma as compared to air would cause total internal reflection of the microwaves. The guided wave must have a frequency lower than the plasma frequency – approximately 300 GHz for a filament [11].

One unique application is filament induced cloud formation and precipitation. During cloud formation, water vapor condenses onto cloud condensation nuclei (CCN). The ions in the filament plasma can serve as additional CCN or attach to pre-existing CCN, making it more active. Additionally, the temperature gradient between air surrounding the filament and the cold atmosphere results in thermal air flow. Convection mixes the air and increases interaction between CCN and water vapor, producing water, ice, and snow [12].

Filamentation can also be used to detect pollutants. Each molecule has a unique spectral ‘fingerprint’. A filament can remotely excite the fluorescence of molecules in the air, which can then be detected with a spectrometer to determine the chemical composition [13]. This technique is called LIDAR (light detection and ranging). In addition, the same concept can be applied to solid targets at long distances, called FIBS (femtosecond laser induced breakdown spectroscopy) [9].

CHAPTER 2 – REFRACTIVE INDEX MODIFICATION BY FILAMENTATION IN AIR

2.1 – Prevalent Filament Measurement Techniques

2.1.1 – Plasma

As described in the previous chapter, there are many potential applications for filamentation, several of which rely on filament plasma formation. Therefore, an accurate diagnostic is necessary to properly characterize the temporal, radial, and axial profile of the plasma channel for use in these applications.

A variety of methods have been employed to study filament plasma dynamics in air. Such techniques include conductivity measurements, acoustic or sonographic detection, interaction with CW microwave propagation, fluorescence molecular spectroscopy, and interaction with THz radiation [14-27]. Three other methods which utilize the refractive index modification of the medium due to filamentation are diffractometry, in-line holography, and interferometry [27-34]. Each of these methods is briefly summarized below. While this is not an exhaustive list of filament plasma measurements, those techniques which procure time-resolved data of filament plasma in air will be reviewed.

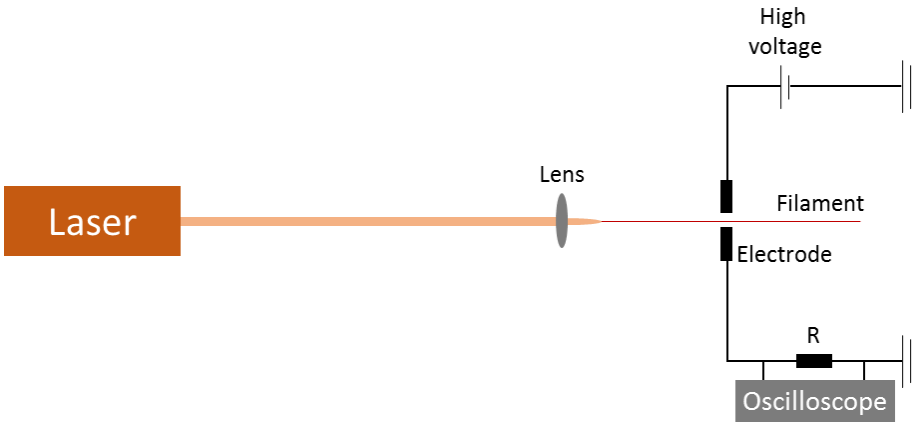

Figure 3: Schematic for the plasma conductivity measurement performed by Abdollahpour, et al. [17]

Several groups have measured plasma dynamics using the conductive properties of filaments [14-21]. For example, Abdollahpour, et al. measured changes in voltage between electrodes due to presence of plasma [17]. In their setup, they placed electrodes on either side of the filament, connected to a high voltage source (see Figure 3). The electrodes induce a polarization in the plasma, which changes the total electric field. The high voltage source then provides charge to the electrodes to maintain a constant voltage. The resulting transient recharge current is measured by an oscilloscope. The signal is proportional to the density. However, this technique must be calibrated by another measurement technique, such as in-line holography. The resolution is also limited by the oscilloscope and thus too low to visualize picosecond recombination dynamics.

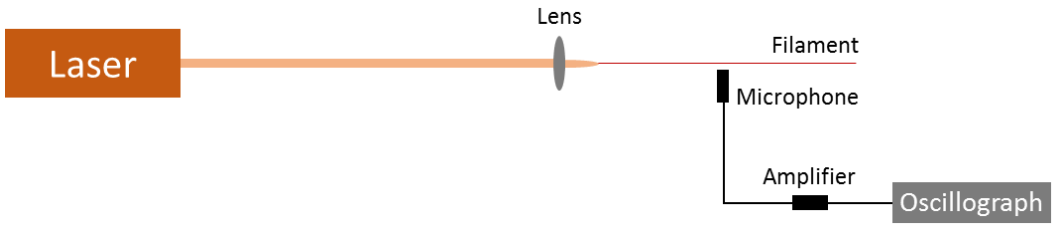

Figure 4: Schematic for the acoustic detection of electron density used by Zuo-Qiang, et al. [22]

Another popular technique is acoustic detection of the sound waves produced by plasma formation. In the experiment performed by Zuo-Qiang, et al., [22] a microphone is placed perpendicular to the plasma channel, at fixed distance from the axis (see Figure 4). The sound is amplified and recorded by an oscilloscope. An expression is derived for the energy of electrons in the channel, by relating the electron generation rate of N_2 and O_2 to the laser intensity and considering the increase in KE of electrons by absorbing laser energy. Another expression is derived for the energy of a sound wave of a segment of filament. These energies are proportional. Rearranging, an expression is obtained for $S_o(z)$, the detected peak voltage signal at location z.

The system is calibrated by assuming a particular peak density. Several assumptions must be made in regards to the plasma properties in order to do the calculations. Again, the temporal resolution is limited by the electronic equipment, so picosecond dynamics are not resolved.

Papeer, et al. measured the temporal evolution of filament plasma density by measuring the interaction of the filament with a continuous microwave source ($\lambda_0 = 1.064\ \mu m$) in a single mode waveguide [23, 24]. This technique does not require precise optical alignment. The decay curve produced by the attenuation in the signal at the MW detector is compared to theoretical simulations based on air chemistry analysis in order to measure plasma density. The temporal and spatial resolution are 0.3 ns and 3 mm respectively.

Another technique for plasma diagnostics is fluorescence molecular spectroscopy. Bernhardt, et al., measured the spectrum of the side-on fluorescence of the filament and analyzed the Stark broadening [25]. The density can be calculated from the Stark broadening line width. The temporal resolution was in the nanosecond regime (~5 ns), and the spatial resolution was about 1 mm. Théberge, et al. used the side-on averaged N_2^+ fluorescence strength as a measure of plasma density [27]. First, the average electron density had to be measured using another technique, longitudinal diffractometry, in order to determine the correlation between signal strength and plasma density. By fitting the longitudinal diffraction of a probe pulse with Fresnel diffraction integral, they were able to obtain the averaged electron density for certain focal lengths and energies. Comparing the averaged electron density with the averaged N_2^+ florescence strength, they determined the appropriate calibration function. They report peak plasma densities down to 10^{13} cm^{-3} and plasma FWHM diameters for four different NA conditions and unassisted focusing,

with spatial resolution of 2 μm along propagation. The inability to obtain temporal information about the plasma is the major shortcoming of this technique.

Bodrov, et al., detected THz probe scattering as a measure of electron density [26]. An infrared probe pulse generated a 1 ps pulse of THz radiation in ZnTe. A bolometer collected scattered light at 90° from the plasma (Figure 5). Scattering decreased as density decreased, since the critical density for THz is on the order of 10^{16} cm^{-3}. Numerical simulation predicted the scattering of THz from a symmetric cylinder of plasma. With initial conditions provided by an interferometric technique, very low plasma densities could be calculated from the THz signal.

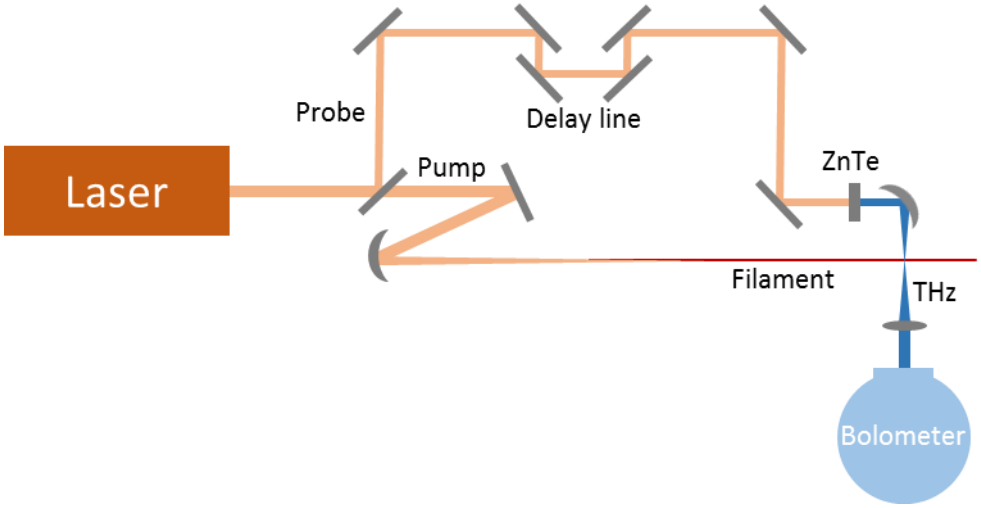

Figure 5: Diagram showing the experimental setup used by Bodrov, et al., [26] in which THz scattering from a filament was measured to determine the electron density of the plasma.

As mentioned previously, diffractometry is another popular technique for measuring filament plasma density, as well as the slight variation on this technique, longitudinal diffractometry [27-29]. Sun, et al. determined the transient electron temperature and density with picosecond resolution by measuring diffraction and absorption of a probe beam to determine the real and imaginary parts of the dielectric constant and applying the Drude model [28].

The technique of in-line holography has also been widely used for filament plasma diagnostic [30-32]. Rodriguez, et al, imaged diffraction patterns produced by a filament in a probe beam [30]. They extracted the electron density using iterative wavefront propagation and were able to measure peak electron densities down to about 2×10^{16} cm^{-3}. Interpretation of the data required estimating the filament transverse length, which they achieved by measuring the side-on fluorescence and recording burn spots.

One other technique that is commonly employed is interferometry [26, 33, 34]. Y. Chen, et al. extracted the phase shift produced in a probe pulse by a filament using interferometry to report electron densities for several positions along the propagation axis, using two different pulse durations, and for several delays at a fixed location [33, 34]. An intersection angle of 0.75° between pump and probe is used to increase sensitivity. They report having a minimum detectable electron density of 5×10^{14} cm^{-3}.

2.1.2 – Kerr Effect

A few groups have attempted to directly measure the Kerr effect associated with filamentation. The primary diagnostic employed by these groups is holography, as described in the previous section. Centurion, et al., compared the propagation of filaments in air, water, and CS_2 [35]. However, the Kerr effect was only measured in the latter two cases. No specific values for this refractive index change are given.

Balciunas, et al., characterized the dynamics of filamentation in water [36, 37]. They found that the peak Δn remained between 0.8 and 1.2×10^{-3} along propagation for four different energies between 0.3 and 27 μJ at an unknown fixed delay between pump and probe [37]. They also

observed the Kerr effect at 0.65 μJ for four delays between 0 and 6600 fs along propagation, with a peak phase shift of 0.3 rad, though the corresponding Δn is not calculated [36].

Siaulys, et al., studied the interaction of two filaments in Sapphire [38]. They reported a peak phase shift of approximately 0.15 rad due to the Kerr effect for pump energies between 2.8 and 4.9 μJ. They focused down to an effective 1/e spot size of 13.4 μm using a 50 mm lens.

Papazoglou, et al., reported a refractive index change due to the Kerr effect in air for four delays from 0 to 1120 fs [32]. Their 35 μJ pump beam was focused using a 0.11 NA, 10x microscope objective. The peak value for Δn reached 2×10^{-3}. This technique is sensitive to refractive index perturbation on the order of 10^{-3}.

Another technique that has been employed to measure the Kerr effect is single-shot supercontinuum spectral interferometry (SSSI). Given the amplitude and spectral phase of the supercontinuum probe, the temporal phase shift of the probe due to interaction with the pump can be determined. Wahlstrand, et al., measured the Kerr effect in Argon, using a pump perpendicular and parallel to the probe for three different input energies [34]. The peak detected phase shift is 0.1 rad, but the corresponding Δn is not reported.

At NA's closer to the transition point to the nonlinear regime [39], the anticipated change in refractive index to the air would be an order of magnitude or two lower than that measurable by holography or interferometry alone. The appropriate sensitivity required to measure the weak Kerr effect and plasma densities is obtainable by changing the crossing geometry between pump and probe as in [33]. This technique enables direct measurement and sufficient sensitivity without complete loss of temporal or radial information.

2.2 – Experimental Design

The goal of this study is to obtain radially and temporally resolved measurements of the filament plasma density at NA's approaching the transition to the nonlinear regime. The variation in the plasma density for different initial parameters will be evaluated. The following sections outline the laser used to produce the filament and the optical systems used to characterize the beam profile and the plasma.

2.2.1 – Multi-Terawatt Filamentation Laser

The laser used in this experiment was the MTFL facility at the Laser Plasma Laboratory. It has three possible outputs. The kilohertz line has a 1 kHz rep rate, 50 fs pulse duration, and 1 mJ energy. The mid-energy line has a 10 Hz rep rate, 50 fs pulse duration, and up to 40 mJ energy. The full-energy line has a 10 Hz rep rate, 50 fs pulse duration, and up to 470 mJ energy.

A Millennia V CW laser at 532 nm pumps the Oscillator, which is a mode-locked, Ti:Sapphire Tsunami laser with a 74 MHz rep rate. The output pulses have an average power of 330 mW with a spectrum centered at 800 nm with 40 nm bandwidth. These pulses are stretched using two passes off a single grating to ~450 ps. Each pass consists of four reflections. A telescope down collimates the beam prior to entering the Dazzler, isolator, and regenerative amplifier. The Dazzler is an acousto-optic programmable dispersive filter (AOPDF). By manipulating the phase and amplitude of the input beam, the output spectrum and dispersion of the laser can be modified. The Dazzler is used to place a dip in the spectrum around 800 nm to prevent some gain narrowing in the regen. Settings for 2^{nd}, 3^{rd}, and 4^{th} order dispersion can be loaded on the Dazzler to counteract the dispersion of the system. The train of pulses is picked down to 1 kHz or 10 Hz before seeding the regenerative amplifier.

The regen uses a Ti:Sapphire crystal as the gain medium. The crystal is pumped from both sides by a Spectra-Physics Evolution-30 laser (1 kHz, 527 nm, 20 W). The seed pulse makes 15-17 round trips in the Z-shaped cavity before being ejected. The timing of the entry and exit of the seed pulse is controlled by Pockels cells. The regen output is spatially cleaned and resized. A flip mirror can send the beam towards a telescope and the kHz compressor.

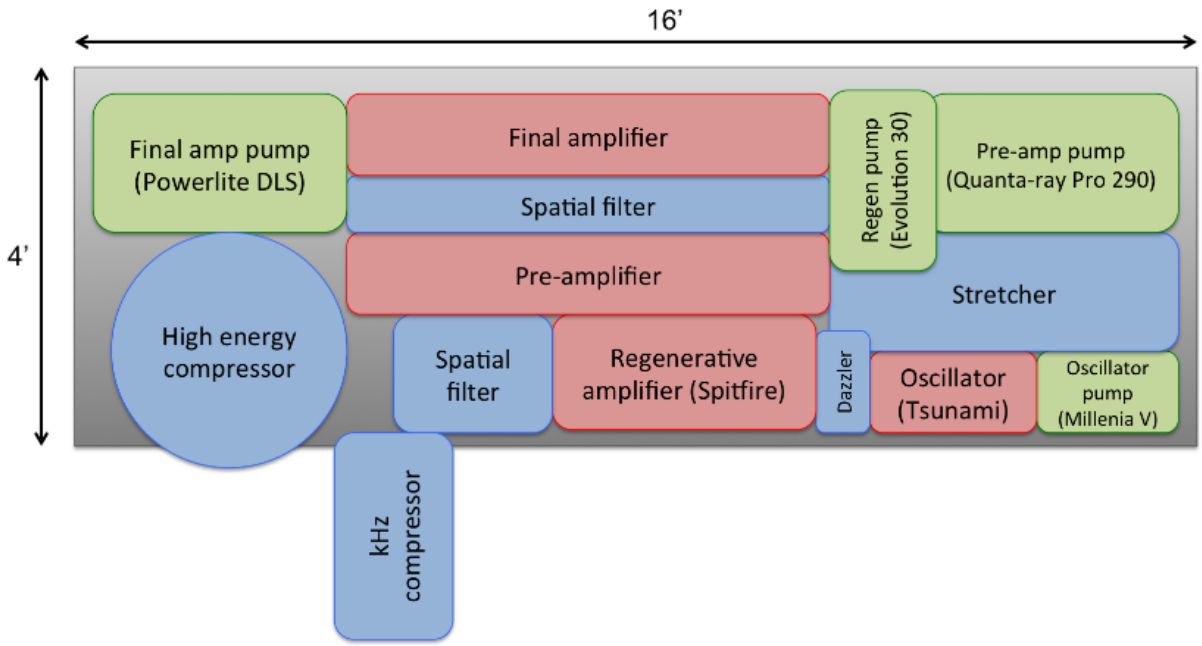

Figure 6: Schematic of the MTFL system [39].

If the flip mirror is down, the beam enters a 6-pass bowtie pre-amplifier. Another Ti:Sapphire crystal is pumped equally from both sides by a Spectra-Physics Quanta-Ray Pro 290 (10 Hz, 532 nm, 750 mJ). The pre-amp output is spatially cleaned. A flip mirror then sends the beam to a telescope to enlarge the beam before entering the high-energy compressor for the mid-energy line. The compressor uses two gratings and a corner reflector.

Changing the flip mirror allows the beam to be further amplified. In the 3-pass bowtie final amplifier, a Ti:sapphire crystal is double pumped by a Continuum Powerlite DLS (532 nm,

2 J). The beam diameter is enlarged by a telescope prior to entering the high-energy compressor. The output of the final amp constitutes the full-energy line.

2.2.2 – Grazing Incidence Imaging System

The grazing incidence imaging system, or Limaging system [39], is used as a diagnostic of the filament beam profile. It can be used within the filament, where peak intensity reaches tens of TW/cm^2. To prevent damage to the CCD at these intensities, a series of 5 wedges, two at 83°, two at 65°, and one at 45°, are used to attenuate the beam by a factor of 10^7. The beam is imaged to the CCD with an f=10 cm lens. ND filters are used to further reduce the intensity as needed.

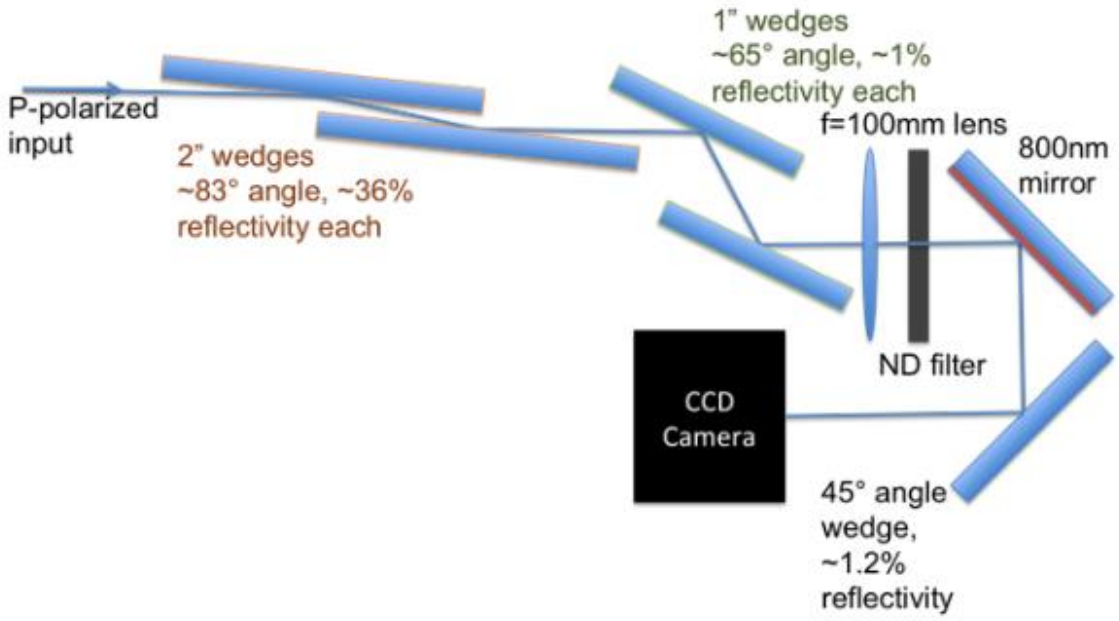

Figure 7: Schematic of the grazing incidence imaging system [39].

2.2.3 – Folded Wavefront Interferometer

The interferometer used to measure the slight phase shift induced by filament plasma is a Michelson type interferometer with an additional reflection in one arm compared to the other arm.

Thus the probe beam overlaps and interferes with the mirror image of itself at the CCD. Since the filament plasma is small compared to the dimensions of the probe beam, the clean portion of one beam interferes with the perturbed portion of the other beam. This design allows for the probe beam to interact with the sample prior to entering the interferometer, which is a necessity given the filament-probe crossing geometry.

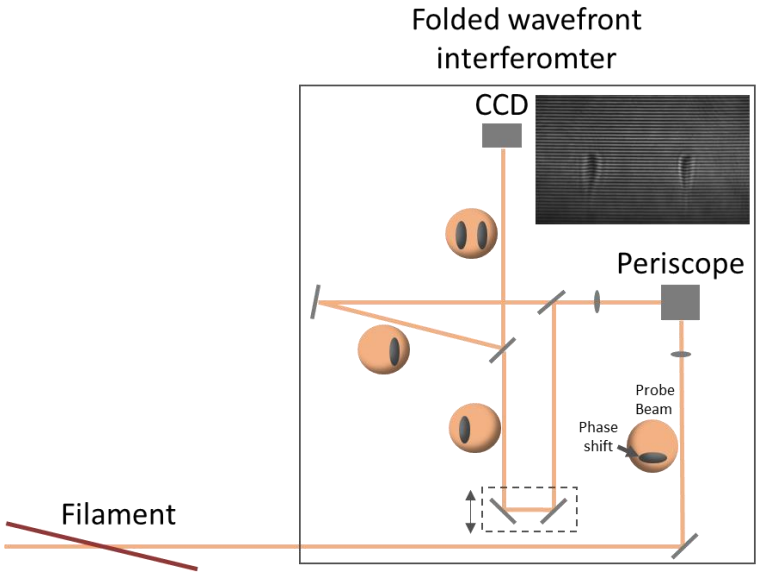

Figure 8: Schematic of the folded wavefront interferometer. The circular cartoons illustrate the probe beam cross section, in which the grey oval indicates the perturbed portion of the beam. The inset shows an example interferogram with duplicate phase information on the left and right hand sides.

2.2.4 – Experimental Setup

The low energy output of the laser (800 nm, 10 Hz, maximum 40 mJ) was used for this experiment. The beam was split into pump and probe beams, using the light reflected from and leaked through a mirror respectively. The pump beam, with an 11.9 mm $1/e^2$ diameter, was focused to create plasma using a 40 cm, 1 m, or 2 m lens. The probe beam (<12 μJ) was cleaned with a spatial filter, since a clean beam profile is crucial to detecting minute changes in phase. Probe and plasma intersected at an angle θ. A small angle (<6°) was used to increase the interaction length

and thus the sensitivity of the measurement. A delay line in the probe beam path was used to control the relative timing between pump and probe. With the probe beam blocked, the Limaging system was used to image the beam profile at different location along the propagation direction. The lenses were mounted on translation stages to easily adjust the location in the plasma that would interact with the probe. A folded wavefront interferometer (see Section 2.2.3) was used to measure the phase shift produced in the probe beam by the presence of the filament. The interaction region was 1:1 imaged to a CCD through the interferometer using a pair of relay lenses. 200 interferograms were saved for each delay, as well as background photos, taken with the pump beam blocked.

Analysis of the phase maps retrieved from interferograms produced by this system have revealed that the standard deviation of the phase is 14.8 μrad. For a 100 μm diameter filament plasma and a 3° crossing angle between pump and probe, this corresponds to a minimum detectable (2σ) refractive index change of 2×10^{-6} or electron density of 6×10^{15} cm^{-3}. These values of course decrease for smaller crossing angles.

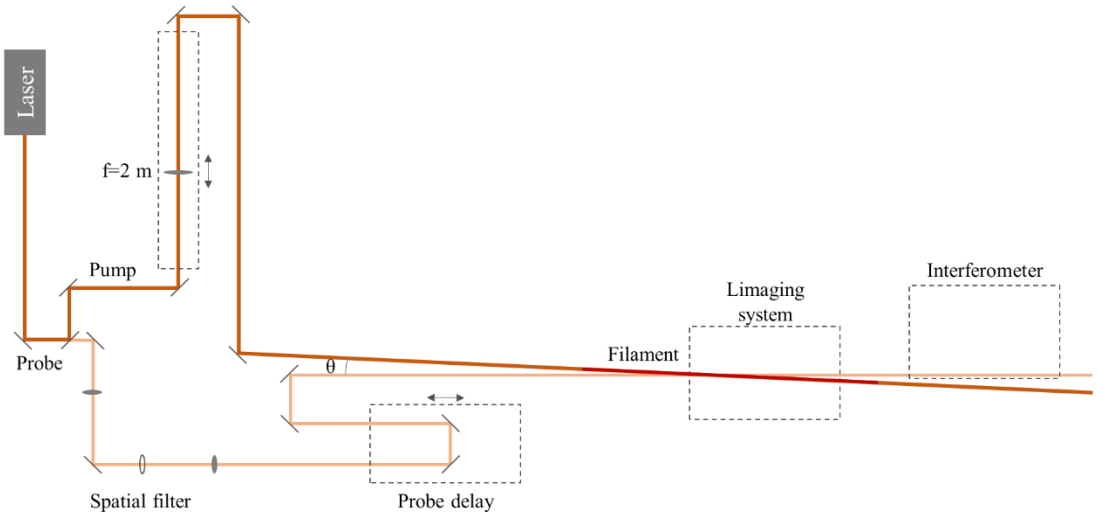

Figure 9: Schematic of the optical system for the time-, space- resolved electron density measurement.

2.3 – Methods of Analysis and Simulation

2.3.1 – Extraction of Electron Density and Kerr Effect

In order to analyze the raw interferograms, the phase information was first extracted following a method proposed by Takeda, et al. [40]. This step was accomplished by taking the 2D Fourier transform of the image, applying a Hann window, and selecting a spectrum to shift to the origin, before taking the inverse Fourier transform. A Hann window [41] is defined as $w(I) = \frac{1}{2}\left(1 - \cos\left(\frac{2\pi I}{N}\right)\right)$, where I, in this case, is the interferogram and N is the number of pixels along the x dimension of the interferogram. The spectrum was chosen by eliminating the DC tone and determining the frequency with the peak intensity, which represents the frequency of fringes in the interferogram. A window of frequencies about that point were selected and centered at the origin, while the intensity of all other frequencies was set to 0 (Figure 10). This process eliminated the fringes and enabled determination of the absolute phase shift.

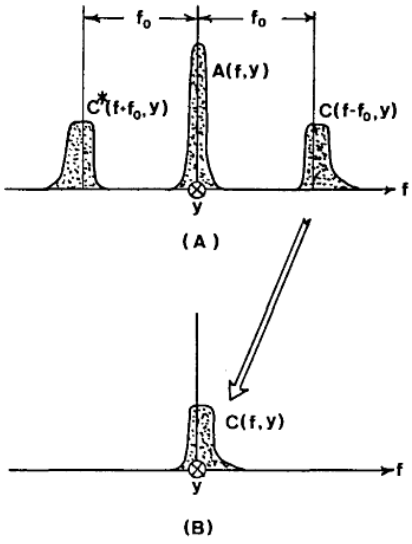

Figure 10: (A) The Fourier spectra of a single lineout of an interferogram, in which A(f, y) is the DC component and C(f-f_0, y) is the phase information of interest, centered at f_0, the spatial frequency of the fringes; (B) The spectrum of interest is selected and translated by f_0 [40].

However, the phase shift is discontinuous upon retrieval. Therefore an algorithm outlined in the paper by Takeda, et al., for removing the discontinuities was employed [40]. In order to determine the location of the discontinuities, the phase step size between adjacent points along one dimension are determined. Then a criterion is applied such that if the difference in phase is less than $-0.9 \times 2\pi$, then 2π is added to the phase at that point and all points following, and if the difference in phase is greater than $0.9 \times 2\pi$, then 2π is subtracted from that point and all points following (Figure 11).

Background removal was achieved by retrieving and averaging over the phase from 10 or more interferograms having no perturbation from plasma and subtracting this from each phase image with plasma. Once the discontinuity is removed and the background subtracted, a single lineout of the 2D phase image is selected, corresponding to the location in the image where the plasma passes through the focal plane of the imaging system in the interferometer. All remaining calculations are performed solely on this lineout of the image.

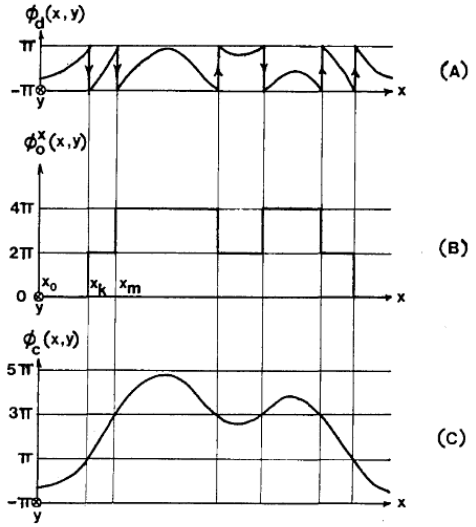

Figure 11: (A) An example discontinuous phase, wrapped between $-\pi$ and π; (B) the phase offset needed to unwrap the phase; (C) the continuous phase after addition of the discontinuous phase and offset [40].

Once the phase has been retrieved and the lineout selected, the refractive index must be calculated. In terms of the refractive index, the difference in phase between the clean portion of the beam and the perturbed portion of the beam is given by Eq. 11, setting n_0 equal to the refractive index of air.

$$\Delta\phi = \int \left(k_{plasma} - k_0\right) dl = \int (n-1)\frac{\omega}{c} dl \qquad (11)$$

where k_{plasma} and k_0 are the wavenumbers for a laser propagating in a medium with and without plasma, n is the refractive index, ω is the angular frequency of the laser, and c is the speed of light. With a negligible magnetic field, the refractive index induced by the plasma is given by

$$n^2 = 1 - \frac{\omega_p^2}{\omega^2} = 1 - \frac{\rho_e}{\rho_c} \qquad (12)$$

where ω_p and ω are the plasma and laser frequencies respectively and ρ_e and ρ_c are the plasma electron density and critical electron density. For electron densities much lower than the critical density, change in n is approximated by Eq. 7 using the binomial approximation, and the phase shift becomes

$$\Delta\phi = \frac{\omega_0}{c}\int \left[\left(1 - \frac{\rho_e}{\rho_c}\right)^{\frac{1}{2}} - 1\right] dl \approx -\frac{\omega_0}{2c\rho_c}\int \rho_e dl \qquad (13)$$

where ρ_e, ρ_c, and c are the same as above and ω_0 is the central laser frequency. If the plasma is assumed to be cylindrically symmetric and if propagation of the probe is perpendicular to the plasma (Figure 12), then the detected phase shift is effectively the integral over a circular cross-section of the plasma, in the y-direction, giving phase shift as a function of x. This integral can be converted to an integral over r.

$$\Delta\phi(x) = \frac{-k_0}{2\rho_c}\int_{-\sqrt{R^2-x^2}}^{\sqrt{R^2-x^2}} \rho_e(r) dy = \frac{-k_0}{\rho_c}\int_x^R \rho_e(r)\frac{r dr}{(r^2-x^2)^{\frac{1}{2}}} \qquad (14)$$

where R is the radius of the region of interest. An equation of the form (14) gives the Abel transform of $\rho_e(r)$. Therefore, $\rho_e(r)$ can be related to $\Delta\phi(x)$ using the inverse Abel transform.

$$\rho_e(r) = \frac{2\rho_c}{\pi k_0}\int_r^R \frac{d(\Delta\phi)}{dx}\frac{dx}{(x^2-r^2)^{\frac{1}{2}}} \qquad (15)$$

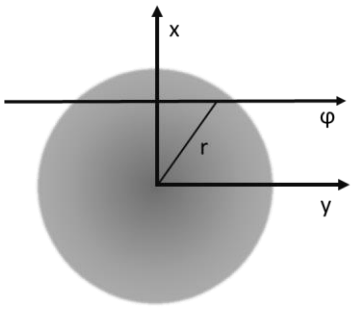

Figure 12: Geometry of this experiment, showing a circular cross-section of the filament plasma, traversed in the y-direction by a probe beam, producing a phase shift as a function of x.

The refractive index produced by the Kerr effect is given by Eq. 1, with $n_0 = 1$ for air. The resulting phase shift is given by Eq. 2, which is the same as Eq. 13 but with $\Delta n_K = n_2 I$ in place of $\Delta n_p = -\frac{\rho_e}{2\rho_c}$. Thus, the radial refractive index change due to the Kerr effect follows the same derivation as above.

$$n_2 I(r) = \frac{-1}{\pi k_0}\int_r^R \frac{d(\Delta\phi)}{dx}\frac{dx}{(x^2-r^2)^{\frac{1}{2}}} \qquad (16)$$

Using the modified discrete Fourier-Hankel method studied by S. Ma, et al., the radial profile of the refractive index in either case can be calculated from the phase shift using the following [42]:

$$\Delta n(r_i) = \frac{1}{k_0}\frac{\alpha^2\pi}{2nR}\sum_{j=-n}^{n-1}\Delta\phi(x_j)\sum_{k=1}^{n/\alpha} kJ_0\left(\frac{\alpha ik\pi}{n}\right)\cos\left(\frac{\alpha jk\pi}{n}\right) \qquad (17)$$

where J_0 is the Bessel function of the first kind and α acts as a lowpass filter. In this equation, j, k, and n are integers over which summation is being performed, and R and k_0 are as described previously. This equation must simply be multiplied by $-2\rho_c$ in order to obtain the radial profile

of the electron density. Once the change in refractive index is retrieved for each interferogram, the output is averaged over 200 images for each delay. Example output of the code is displayed in Figure 13.

However, since the propagation of the probe is not perpendicular to the plasma, the cross-section probed is elliptical rather than circular. Therefore, the results determined using the method described thus far would over-estimate the density or Kerr effect by attributing the accumulated phase shift to a much smaller region along one axis. Kreye, et. al, derived an expression for a modified Abel inversion that assumes elliptical symmetry [43]. The ultimate difference in calculation amounts to multiplication of the result by the factor b/a, where a and b are the semi major and semi minor axes of the ellipse respectively. In this case, a and b are related by the geometry shown in Figure 14; therefore the factor is simply $\sin(\theta)$. This corresponds to a multiplicative factor of 0.05 for a 3° crossing angle and 0.03 for a 1.7° angle.

This discussion may raise a concern that the radius retrieved is no longer truly the radius but rather some other variable more descriptive of an ellipse. However, in this particular case, the plasma itself is cylindrically symmetric, so it is as if a circular cross-section of the plasma were stretched out to form the observed ellipse. Thus the 'radial' profile attributed to the ellipse is equivalent to the radial profile of a circular cross-section of the filament, assuming uniformity of the cylinder within the region observed. If the filament does not resemble a uniform cylinder in the observed region, then the multiplicative factor may fall between that predicted for an ellipse and a circle (between $\sin(\theta)$ and 1), and the radial profile will only approximate the true cross-section.

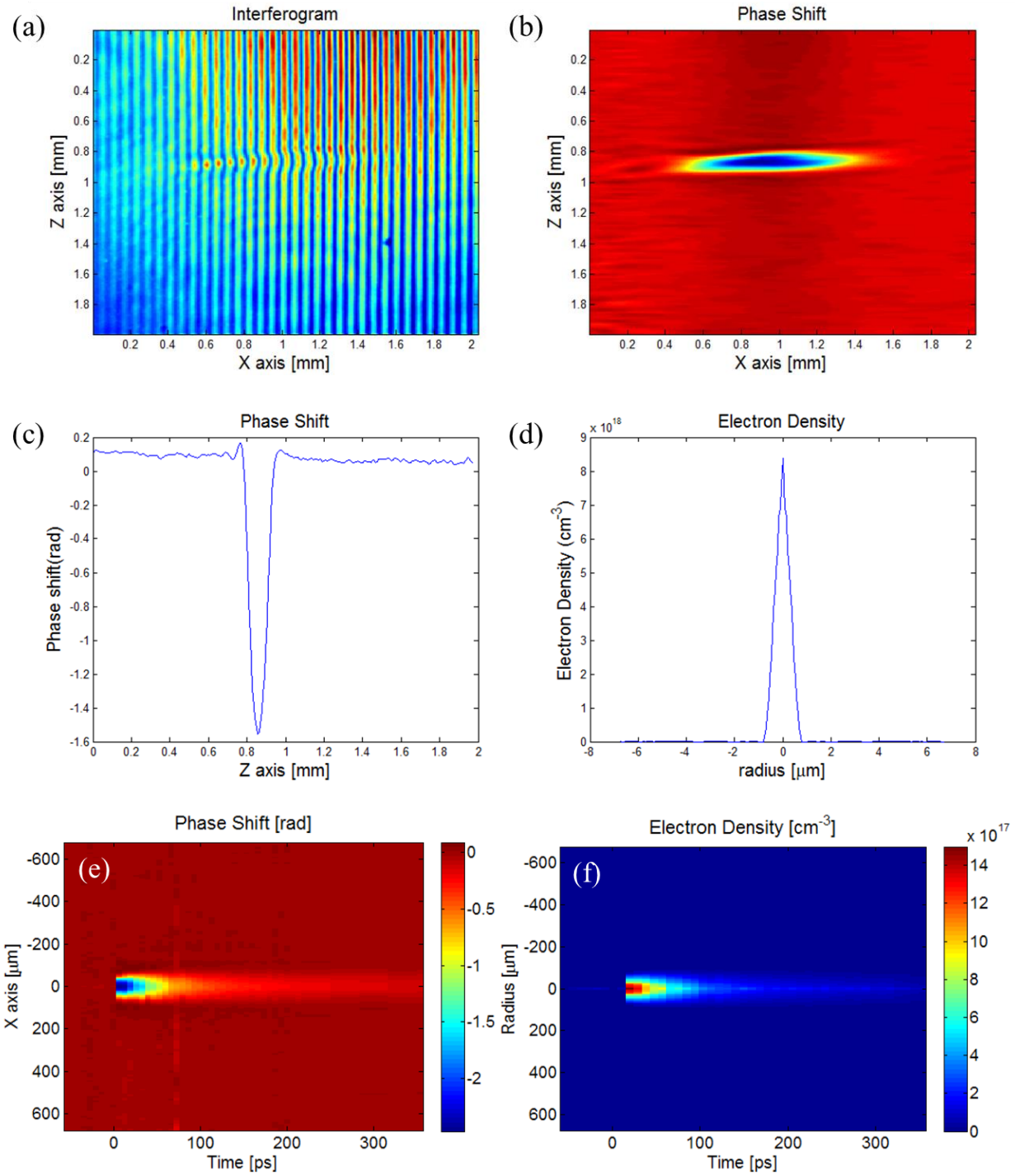

Figure 13: Plots demonstrating the steps followed in the code for retrieving the electron density. First the phase is retrieved form the raw interferogram (a to b), then the central lineout is selected (c), then Abel inversion is performed (d). (e) The phase shift for all measured delays, which after Abel inversion gives (f).

Before applying the factor to the raw data, the multiplicative factor will first be confirmed by comparison of experiment with the simulated plasma decay. The peak electron density from the uncorrected data will be multiplied by the factor predicted by the angle and input as the initial value in the simulation. The output of the code will then be divided by this same factor and compared with the experimental results to determine how well they agree. Once verified, the factor will be applied to the raw data and removed from the simulation.

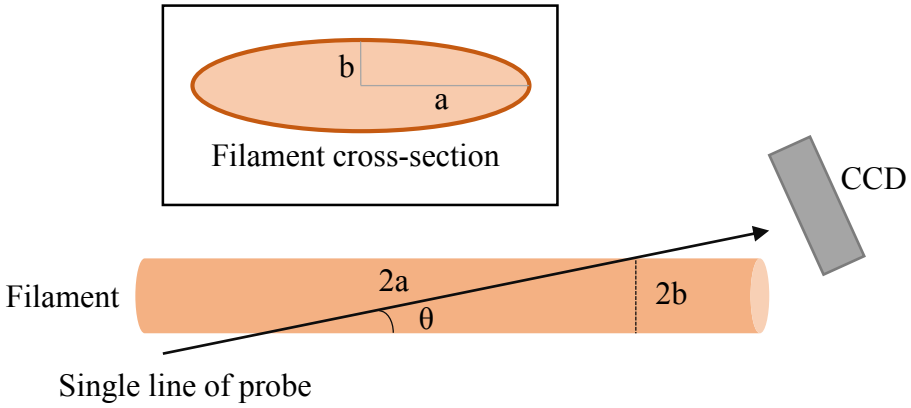

Figure 14: Diagram showing the intersection between pump and probe, revealing an elliptical cross-section with semi major and semi minor axes a and b respectively.

2.3.2 – Simulation of Filament Propagation

An in-house code, written by K. Lim [39], was used to simulate filament propagation. The code numerically solves the nonlinear Schrodinger equation (NLSE) using a split-step method. The code assumes rotational symmetry. It stores the electric field of the laser in a 2D mesh, radius vs. time, and simulates the pulse evolution along propagation. The NLSE is given by the following:

$$\frac{\partial \varepsilon}{\partial z} = \frac{i}{2k}\nabla_{\perp}^{2}\varepsilon - \frac{ik''}{2}\frac{\partial^{2}\varepsilon}{\partial t^{2}} + ik_{0}n_{2}(1-f)|\varepsilon|^{2}\varepsilon + ik_{0}n_{2}f\left[\int_{-\infty}^{t} R(t-t')|\varepsilon(t')|^{2}dt'\right]\varepsilon -$$

$$\frac{\sigma}{2}(1+i\omega_{0}\tau_{c})\rho\varepsilon - \frac{\beta_{K}}{2}|\varepsilon|^{2K-2}\left(1-\frac{\rho}{\rho_{nt}}\right)\varepsilon \qquad (18)$$

In the above equation, the first term on the right hand side describes the effects of diffraction, where ε is the electric field and k is the wavenumber of the medium. The second term incorporates the effect of group velocity dispersion (GVD), k''. The third and fourth terms represent the instantaneous Kerr effect and delayed Raman-Kerr effect, where k_0 is the wavenumber in vacuum and n_2 is the nonlinear refractive index. The factor of f attributes a portion of the Kerr effect to the instantaneous electronic response and the remainder to the delayed molecular Raman response. This molecular response is described by $R(t) = \frac{\Gamma^2 - \omega_R^2}{\omega_R^2} e^{-\Gamma t} \sin(\omega_R t)$, where Γ^{-1} is the molecular response time and ω_R is the molecular rotational frequency. Typical values for these factors in atmospheric conditions are $\Gamma = 1/70$ fs and $\omega_R = 16 \times 10^{12}$ s^{-1}, and $f = 0.5$ has been shown to provide a good fit [39]. The fifth term on the right hand side describes plasma absorption and defocusing, where σ is the cross-section for inverse Bremsstrahlung, τ_c is the electron collision time, ω_0 is the laser central angular frequency, and ρ is the electron density. The final term provides a description of the MPI losses, where $\beta_K = K\hbar\omega_0\rho_{nt}\sigma_K$ is the MPI coefficient, σ_k and K are the ionization cross-section and the number of photons simultaneously absorbed respectively, and ρ_{nt} is the density of neutrals.

To model the evolution of the electron density during filamentation, the code incorporates the following equation:

$$\frac{\partial \rho}{\partial t} = \sigma_K I^K (\rho_{nt} - \rho) + \frac{\sigma}{U_i} \rho I \qquad (19)$$

The first term on the right hand side describes multiphoton ionization. As mentioned previously, K is the number of photons simultaneously absorbed, and MPI scales with intensity, I. The photon ionization cross-section is given by σ_K ($= 2.81 \times 10^{-96}$ W^{-8}cm^{16}s^{-1} for O_2), and the density of

neutrals is given by ρ_{nt} ($= 0.54 \times 10^{19}$ cm^{-3} for 20% O_2 in air) [39]. The second term on the right hand side describes avalanche ionization. The cross-section for inverse Bremsstrahlung is given by $\sigma = \frac{k_0}{n_0 \rho_c} \frac{\omega_0 \tau_c}{1+\omega_0^2 \tau_c^2}$, where $\tau_c \approx 350$ fs is the electron collision time, and the ionization potential is represented by U_i. For simulation in air, the ionization potential for oxygen (12 eV) is taken into account while nitrogen (15.5 eV) is neglected, since oxygen has the lower ionization potential and thus will be first to undergo MPI. For $\lambda_0 = 800$ nm, the number of photons K needed to overcome U_i is 8.

Tunneling ionization is neglected in the ionization rate above since MPI is the dominant mechanism of photoionization in filamentation, as can be shown by the Keldysh parameter. For $\lambda_0 = 800$ nm in air, $\gamma \approx 1.8$. Though this value is not significantly greater than 1, approximation of the ionization rate using MPI and neglecting tunneling ionization has agreed well with experiment. For further details on how the code operates, refer to K. Lim's thesis [39].

2.3.3 – Simulation of Plasma Decay

To model the decay of the plasma electron density in air, only select chemical reactions were taken into account (Table 1). As outlined by Bodrov, et. al, these reactions account for the bulk of plasma dynamics in the short time (~2 ns) following filament formation [26]. Electron recombination occurs through three-body electron recombination with O_2^+ (reaction 0), dissociative electron recombination with O_2^+ (reaction 1), and dissociative electron recombination with complex positive ions (reactions 2-4). Complex ion formation is described by reactions 5-11. A humidity of 50% is assumed for the simulation.

Table 1: List of reactions used in the simulation of plasma decay [26].

NO.	REACTION	RATE COEFFICIENT
0	$e^- + O_2^+ + e^- \rightarrow O_2 + e^-$	$6.1 \times 10^{-20} \left(\frac{300}{T_e}\right)^{\frac{9}{2}} cm^6/s$
1	$e^- + O_2^+ \rightarrow O + O$	$1.95 \times 10^{-7} \left(\frac{300}{T_e}\right)^{0.7} cm^3/s$
2	$e^- + O_2^+ N_2 \rightarrow N_2 + O_2$	$1.3 \times 10^{-6} \left(\frac{300}{T_e}\right)^{\frac{1}{2}} cm^3/s$
3	$e^- + O_4^+ \rightarrow O_2 + O_2$	$4.2 \times 10^{-6} \left(\frac{300}{T_e}\right)^{\frac{1}{2}} cm^3/s$
4	$e^- + O_2^+ H_2O \rightarrow O_2 + H_2O$	$2 \times 10^{-6} \left(\frac{300}{T_e}\right)^{\frac{1}{2}} cm^3/s$
5	$O_2^+ + 2N_2 \rightarrow O_2^+ N_2 + O_2$	$0.9 \times 10^{-30} \left(\frac{300}{T}\right)^{2} cm^6/s$
6	$O_2^+ N_2 + N_2 \rightarrow 2N_2 + O_2^+$	$1.1 \times 10^{-6} \left(\frac{300}{T}\right)^{5.3} e^{-\frac{2357}{T}} cm^3/s$
7	$O_2^+ + 2O_2 \rightarrow O_4^+ + O_2$	$2.4 \times 10^{-30} \left(\frac{300}{T}\right)^{3.2} cm^6/s$
8	$O_4^+ + O_2 \rightarrow O_2^+ + 2O_2$	$3.3 \times 10^{-6} \left(\frac{300}{T}\right)^{4} e^{-\frac{5030}{T}} cm^3/s$
9	$O_2^+ N_2 + O_2 \rightarrow O_4^+ + N_2$	$10^{-9}\ cm^3/s$
10	$H_2O + O_2^+ + O_2 \rightarrow O_2^+ H_2O + O_2$	$2.8 \times 10^{-28}\ cm^6/s$
11	$H_2O + O_2^+ + N_2 \rightarrow O_2^+ H_2O + N_2$	$2.8 \times 10^{-28}\ cm^6/s$

The rate equations for the reactions listed in Table 1 [26] can be written using a Peterson Matrix:

$$\begin{pmatrix} \frac{d[O_2^+]}{dt} \\ \frac{d[O_2^+N_2]}{dt} \\ \frac{d[O_4^+]}{dt} \\ \frac{d[O_2^+H_2O]}{dt} \\ \frac{d[O_2]}{dt} \\ \frac{d[N_2]}{dt} \\ \frac{d[H_2O]}{dt} \\ \frac{d[O]}{dt} \\ \frac{d[e]}{dt} \end{pmatrix} = \begin{bmatrix} -1 & -1 & 0 & 0 & 0 & -1 & 1 & -1 & 1 & 0 & -1 & -1 \\ 0 & 0 & -1 & 0 & 0 & 1 & -1 & 0 & 0 & -1 & 0 & 0 \\ 0 & 0 & 0 & -1 & 0 & 0 & 0 & 1 & -1 & 1 & 0 & 0 \\ 0 & 0 & 0 & 0 & -1 & 0 & 0 & 0 & 0 & 0 & 1 & 1 \\ 1 & 0 & 1 & 2 & 1 & 1 & 0 & -0 & 1 & -1 & 0 & 0 \\ 0 & 0 & 1 & 0 & 0 & -2 & 1 & 0 & 0 & 1 & 0 & 0 \\ 0 & 0 & 0 & 0 & 1 & 0 & 0 & 0 & 0 & 0 & -1 & -1 \\ 0 & 2 & 0 & 0 & 0 & 0 & 0 & 0 & 0 & 0 & 0 & 0 \\ -1 & -1 & -1 & -1 & -1 & 0 & 0 & 0 & 0 & 0 & 0 & 0 \end{bmatrix} \begin{pmatrix} k_0[O_2^+][e]^2 \\ k_1[O_2^+][e] \\ k_2[O_2^+N_2][e] \\ k_3[O_4^+][e] \\ k_4[O_2^+H_2O][e] \\ k_5[O_2^+][N_2]^2 \\ k_6[O_2^+N_2][N_2] \\ k_7[O_2^+][O_2]^2 \\ k_8[O_4^+][O_2] \\ k_9[O_2^+N_2][O_2] \\ k_{10}[H_2O][O_2^+][O_2] \\ k_{11}[H_2O][O_2^+][N_2] \end{pmatrix} \quad (20)$$

where k_i is the rate constant for the ith reaction. The concentration of each species is in units of [cm^{-3}]. As can be noted above, the rate coefficients are highly temperature dependent. The gas temperature T is assumed to be 293 K. The electron temperature T_e is determined by simultaneously solving the electron energy conservation equation [26]:

$$\frac{dT_e}{dt} = \frac{2}{3}\left[-\frac{3}{2}(T_e - T)\nu_e(T_e) + Ik_0[O_2^+][e] - T_e^2\frac{dk_0}{dT_e}[O_2^+][e] - T_e^2\left(\frac{dk_1}{dT_e}[O_2^+] + \frac{dk_2}{dT_e}[O_2^+N_2] + \frac{dk_3}{dT_e}[O_4^+] + \frac{dk_4}{dT_e}[O_2^+H_2O]\right)\right] \quad (21)$$

where ν_e is the frequency of electron energy relaxation in collisions with other molecules and I is the ionization energy of O_2. The second term describes the heating of free electrons due to the energy released in three-body recombination. Together, the second through fourth terms describe the effect of recombination heating. The electron temperature at t=0 is assumed to be 3 eV [26]. The initial value has little bearing on the results, since ν_e decreases dramatically as electron

temperature decreases. The frequency ν_e is determined by comparison with the work done by Ankohin, et. al, using the plot below [44]. Sample output of the code is displayed in Figure 16.

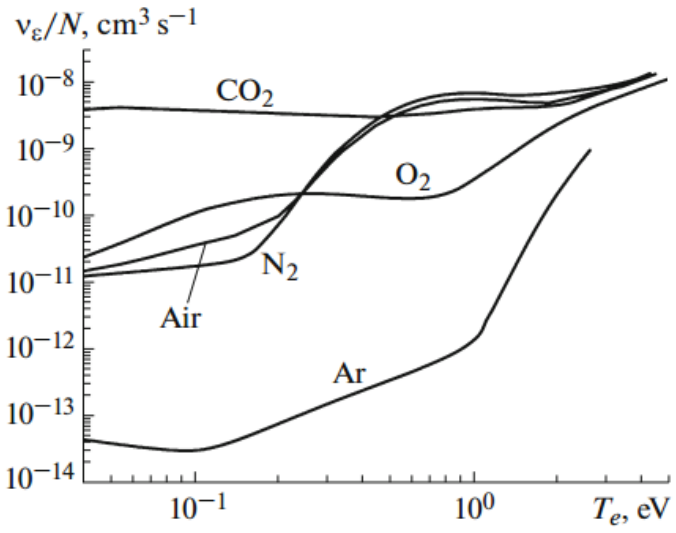

Figure 15: plot of the frequency of electron energy relaxation over the density of neutrals as a function of electron temperature [44].

When performing the experiment, the probe beam is not a delta function and does not have infinite temporal accuracy. In reality, the data is smeared out in time, according to the duration of the probe pulse. Therefore to mimic this 'smearing' of the data, the following procedure was used. First, generate a Gaussian distribution with a peak of one and FWHM equal to the pulse duration, centered at a particular time. Multiply the simulation by this Gaussian, sum over the values, and divide by the sum of the Gaussian. Plot this weighted average as the value for that time. Shift the Gaussian by the time step size taken in the data, and repeat. This same procedure was applied to the results of the NLSE code (developed by Khan Lim).

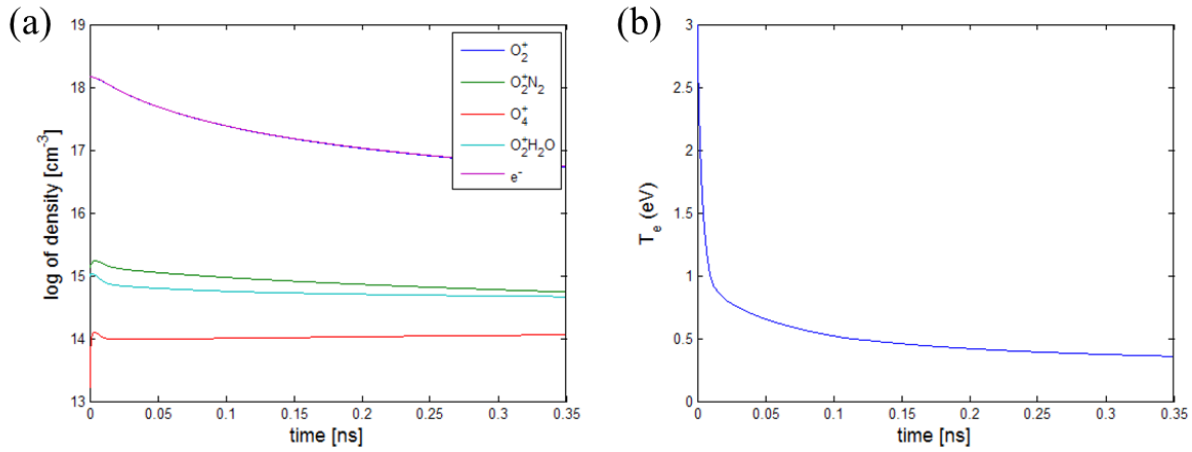

Figure 16: Plots displaying the output of the decay simulation code for an initial electron density of 1.5e18 cm^{-3}. (a) Log plot showing the decay of the electron density and O_2^+ ions, as well as the formation and decay of other complex positive ions. (b) The decay of the electron temperature.

CHAPTER 3 – TEMPORALLY RESOLVED PHASE DIAGNOSTICS OF A FILAMENT

3.1 – Plasma Density

As described in Chapter 1, several of the applications of filamentation exploit the plasma. The plasma channels formed are weakly ionized, with densities on the order of 10^{16} cm^{-3} and could be used to induce corona discharge in clouds or guide microwave radiation. However, use for these applications requires an accurate characterization of the plasma dynamics. In this section, a series of experiments are performed to assess the plasma dynamics under different conditions.

Each dataset displays the temporal evolution of the plasma at only a single location along filament propagation: the focal plane of the lens inducing filamentation. All of the NA conditions considered fall in the linear focusing regime (NA>4.3×10^{-3}) [39]. In this regime, the Kerr effect plays a minimal role in beam propagation, and geometrical focusing is the dominant focusing mechanism governing filamentation. In this regime, there is less supercontinuum generation, no intensity clamping, and a shift in the filament start location [39].

3.1.1 – Varying Numerical Aperture

Experiments were performed to observe the effect of changing numerical aperture on the plasma density. For the first study, the pump energy was fixed at 3 mJ, with a pulse duration of 65 fs. With a FWHM beam diameter of 14 mm ($1/e^2$ diameter of 11.9 mm), measurements were taken using three focal lengths to induce plasma generation: 40 cm, 1 m, and 2 m. These correspond to numerical apertures ($\times 10^{-3}$) of 29.7, 11.9, and 5.9. Data was taken out to a delay of between 0.2-0.35 ns in increments of ≥ 7 ps. For the 40 cm lens, data was taken with a ~5° crossing angle between pump and probe, while a 3° angle was used for the 1 m lens and 1.7° angle for the 2 m

lens. The results are plotted in Figure 17. The decay simulation for each NA is plotted as the red line in Figure 17(b), (d), and (f).

For the second study, the pump beam energy was fixed at 5 mJ, with the same beam conditions as in the previous case. Two focal lengths were used: 40 cm and 2 m. Again a ~5° crossing angle was used for the 40 cm lens, while 1.7° was used for the 2 m lens. Data was taken out to a delay of ~0.35 ns, in steps of 7 ps or more. The results are displayed in Figure 18 for comparison. The fit of the simulation to the decay for both NA's is depicted in Figure 18(b) and (d). In both datasets for varying numerical aperture, a trend of increasing peak density with increasing NA could be noted (Table 2 and Table 3). Similarly, the decay time decreased with increasing NA. These observations confirm that intensity and plasma density clamping do not occur in the linear focusing regime.

In the decay simulation, the rate of three-body recombination for O_2^+ ions was primarily responsible for disagreement between simulation and experiment. As explained by Bodrov, et. al., the rate of two-body dissociative recombination of O_2^+ is well known, and the more complex ions have not yet formed at early times [19]. Therefore, the rate of three-body recombination of O_2^+ was adjusted to determine the value that produced best agreement with the data. The value of $6.1 \times 10^{-20}(300/T_e)^{9/2}$ cm^6/s used by Bodrov, et. al, in [26] appeared to provide good fit to the data.

The necessary multiplicative factor was confirmed for each crossing geometry. For a measured 5° crossing angle, the expected factor of 0.09 provided good fit to the data for one case, but a factor of 0.1 (corresponding to 5.7°) was required for the second case. Due to the small change in angle that occurred between these datasets, a slight variation in the factor was

anticipated. For a measured 3° crossing angle, the expected factor of 0.05 provided good agreement. For a measured 1.7° crossing angle, the predicted factor of 0.03 proved accurate.

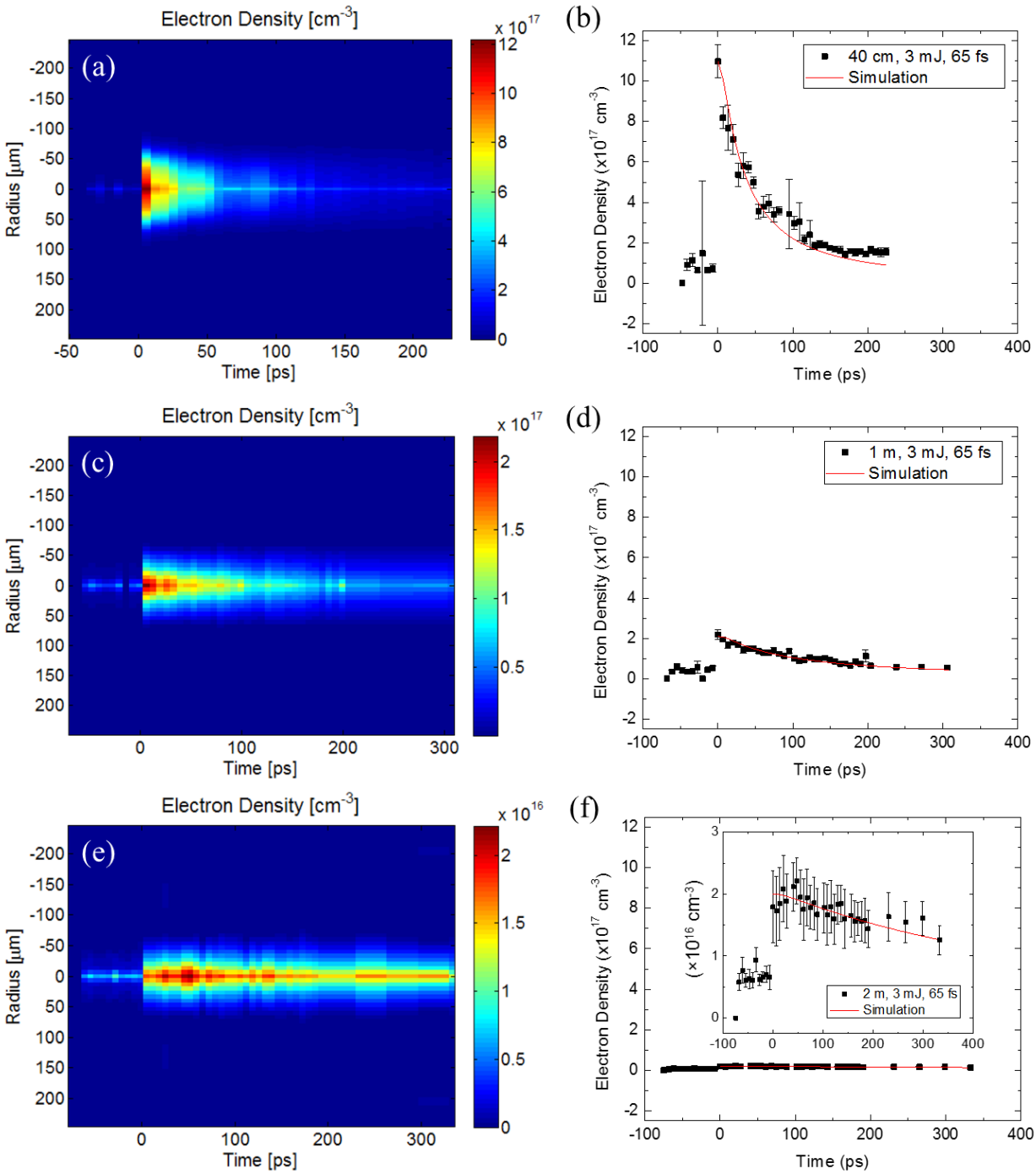

Figure 17: Plots of the electron density of laser induced plasma formation (E=3 mJ, τ=65 fs, ω=11.9 mm) showing (Left) the radial profile of the plasma vs. time and (Right) the on-axis electron density vs. time, both experimental (squares) and simulated (red line). Data collected at the geometrical focus for plasma induced using focal lengths of (a-b) 40 cm, (c-d) 1 m, and (e-f) 2 m.

Table 2: Peak density and half-life of the laser induced plasma (E=3 mJ, τ=65 fs, ω=11.9 mm) measured for NA's ($\times 10^{-3}$) of 30, 12, and 6.

Focal length (m)	Pulse duration (fs)	Energy (mJ)	Crossing angle	Peak density (cm^{-3})	Half-life (ps)
0.41	57	3.03±0.045	5°	1.1e18	34.2
1.1	65	2.96±0.072	3°	2.1e17	98.5
2.2	65	2.99±0.074	1.7°	2.0e16	523

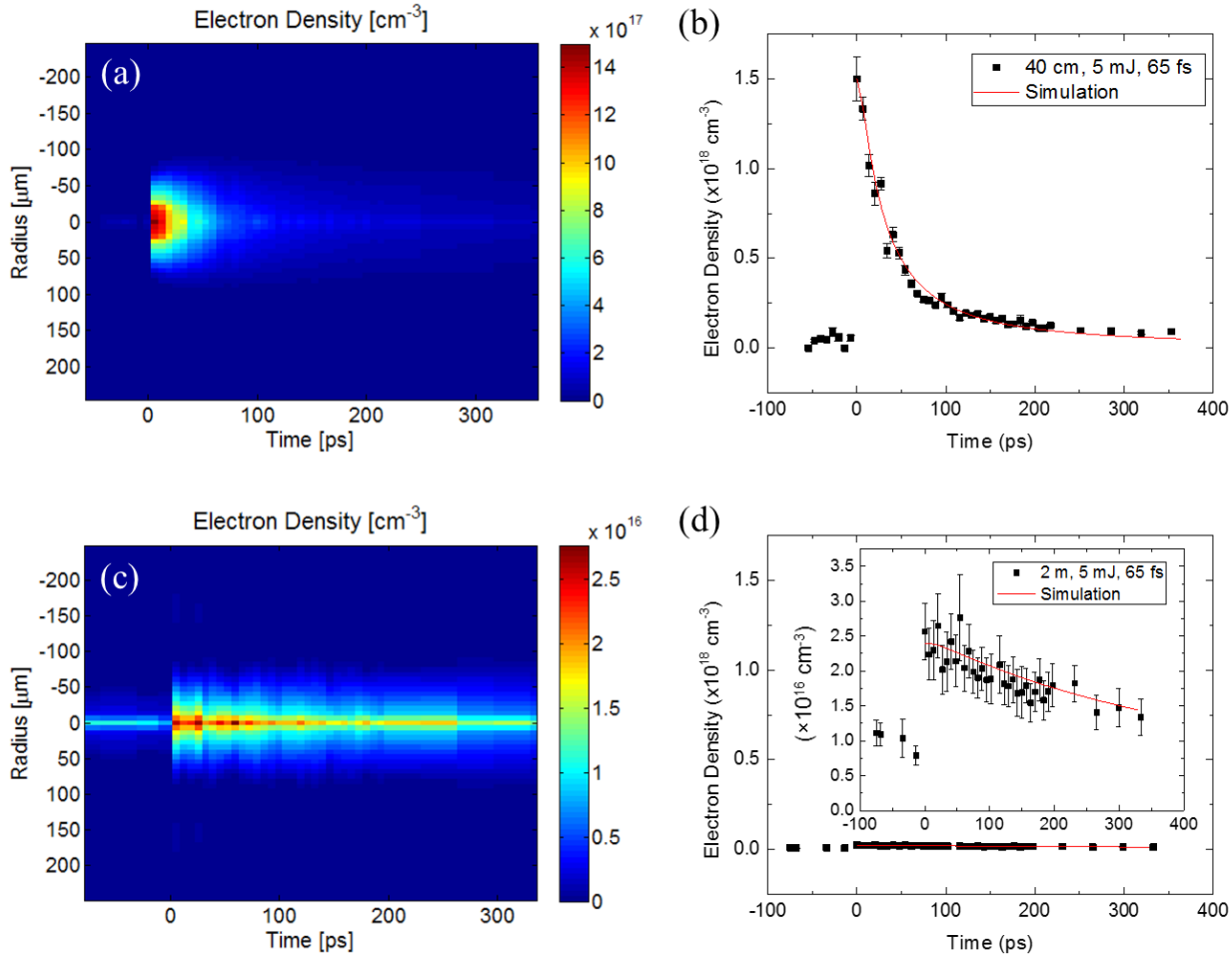

Figure 18: (Left) Plots of the radial profile of electron density vs. time for the conditions in the corresponding plot to the right. (Right) Plots of the on-axis electron density vs. time. Plasma generated using (a-b) 40 cm and (c-d) 2 m lenses to focus the laser (Beam conditions: E=5 mJ, τ=65 fs, ω_0=11.9 mm). Data taken at the geometric focus.

Table 3: Peak density and half-life of the laser induced plasma (E=5 mJ, τ=65 fs, ω=11.9 mm) measured for NA's ($\times 10^{-3}$) of 30 and 6.

Focal length (m)	Pulse duration (fs)	Energy (mJ)	Crossing angle	Peak density (cm^{-3})	Half-life (ps)
0.41	57	4.96 ± 0.078	5.7°	1.5e18	29.2
2.2	65	5.11 ± 0.146	1.7°	2.4e16	464

3.1.2 – Varying Energy

To observe the effect of initial energy on plasma density, the NA was fixed while energy was varied. Again the pulse duration and FWHM of the beam were 65 fs and 14 mm respectively. For the first set of experiments, a focal length of 40 cm was used with a ~5° pump-probe crossing geometry. Three initial energies were used: 0.8 mJ, 3 mJ, and 5 mJ. Temporal measurements were carried out between 0.2 and 0.38 ns, in increments of 7 ps or more. The results are displayed in Figure 19. The decay simulations and fits to the data are displayed in Figure 19(b) and (d). Though the simulation predominantly agreed with the data, one feature that is not described by this model is the appearance of a secondary peak in density at around 100 ps, which is most notable in Figure 19(right). The reason for this additional peak is still under investigation. Comparing the measurements, the peak density increased and the decay time decreased with increasing energy (Table 4). Again, intensity and plasma density clamping were not observed for these focusing conditions.

For the second set of experiments, a focal length of 2 m was used with a 1.7° pump-probe crossing angle, while the energy was changed from 3 to 5 mJ. Measurements were made in increments of $\geq$ 7 ps, out to a delay of ~0.35 ns (Figure 20). The decay simulations and fit of the simulation to the data are shown in Figure 20(b) and (d). It must be noted that for the 2 m lens, the

density only slightly increased (see Table 5), or remained the same within the error, when going from 3 to 5 mJ, suggesting that variations in initial parameters becomes less impactful as the transition point is approached.

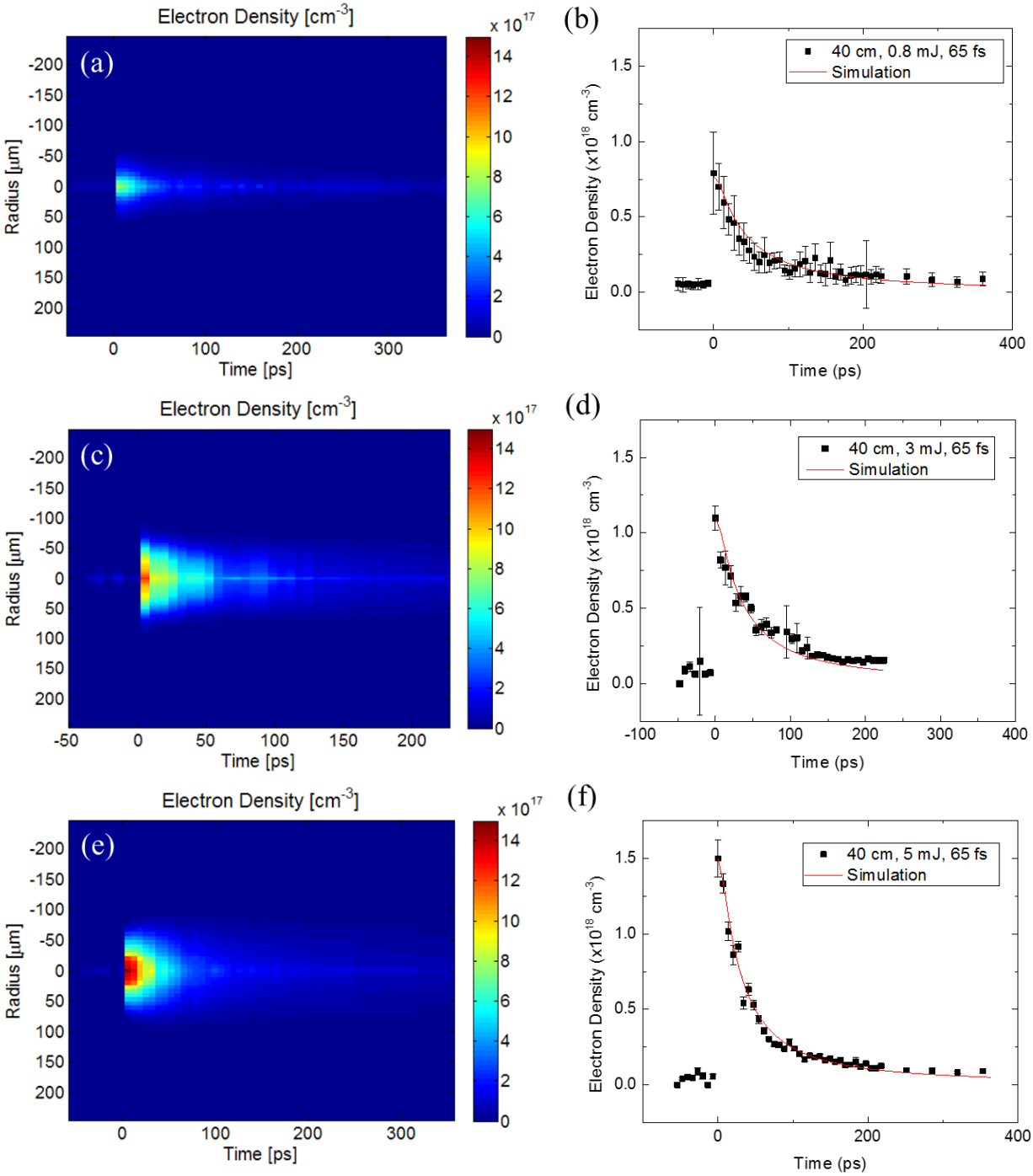

Figure 19: (Left) Plots of the temporal evolution of the radial profile of the electron density at the geometric focus for a plasma channel induced using an f=40 cm lens (τ=65 fs, ω_0=11.9 mm) to focus the laser. (Right) Plots of the on-axis electron density vs. time for the same beam conditions as in the plots to the left. The beam energy prior to plasma generation was (a-b) 0.8 mJ, (c-d) 3 mJ, and (e-f) 5 mJ.

Table 4: Peak density and half-life of the plasma channel induced using an f=40 cm lens (τ=65 fs, ω=11.9 mm) measured for energies of 0.8, 3, and 5 mJ.

Energy (mJ)	Focal length (m)	Pulse duration (fs)	Crossing angle	Peak density (cm^{-3})	Half-life (ps)
0.800±0.014	0.41	65	5.7°	7.7e17	42.7
3.03±0.045	0.41	57	5°	1.1e18	34.2
4.96±0.078	0.41	57	5.7°	1.5e18	29.2

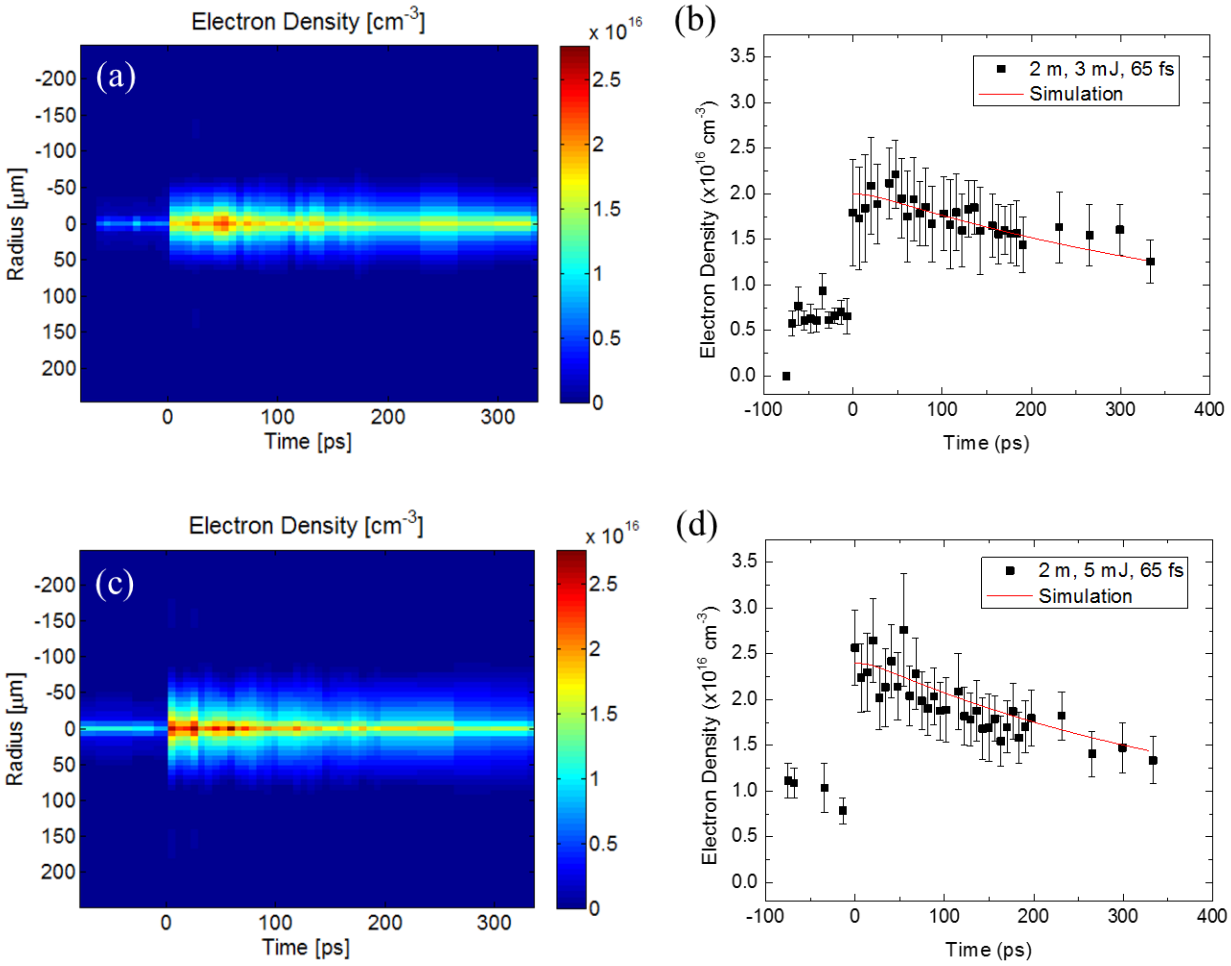

Figure 20: (Left) Temporal evolution of the radial profile of the laser induced plasma density, produced using an f=2m lens (τ=65 fs, ω_0=11.9 mm). (Right) Plots of the temporal evolution of the on-axis electron density for the same beam conditions. Data taken at the geometric focus, with pump beam energies of (a-b) 3 mJ and (c-d) 5 mJ.

Table 5: Peak density and half-life of the plasma channel induced using an f=2 m lens (τ=65 fs, ω=11.9 mm) measured for energies of 3 and 5 mJ.

Energy (mJ)	Focal length (m)	Pulse duration (fs)	Crossing angle	Peak density (cm^{-3})	Half-life (ps)
2.99±0.074	2.2	65	1.7°	2.0e16	523
5.11±0.146	2.2	65	1.7°	2.4e16	464

3.1.3 – Varying Pulse Duration

With fixed focal length and energy conditions, the pulse duration was varied to consider its impact on the plasma density. Using a 2 m lens (NA=5.9×10^{-3}) and a beam energy of 3 mJ, the temporal evolution of the electron density was measured for a 65 fs pulse and a 100 fs pulse. Measurements were made out to delays between 0.3 and 0.6 ns in steps of 0.7 ps or more (Figure 21). The decay simulations and fit to the data are shown in Figure 21(b) and (d). For the final dataset, the angle was not precisely measured but known to be less than 1.7°, the appropriate factor was revealed by simulation to be 0.014, corresponding to a 0.8° crossing geometry.

Increasing pulse duration caused an increase in the peak plasma density and decrease in the decay time (Table 6). This observation is counterintuitive. Since the intensity appeared to be clamped for this NA from previous measurement (Figure 20), the plasma density would be expected to remain the same, or else the plasma density would decrease with the decrease in intensity. However, it may be that the pulse duration of 100 fs is approaching the optimum pulse duration for plasma formation, when considering molecular alignment effects.

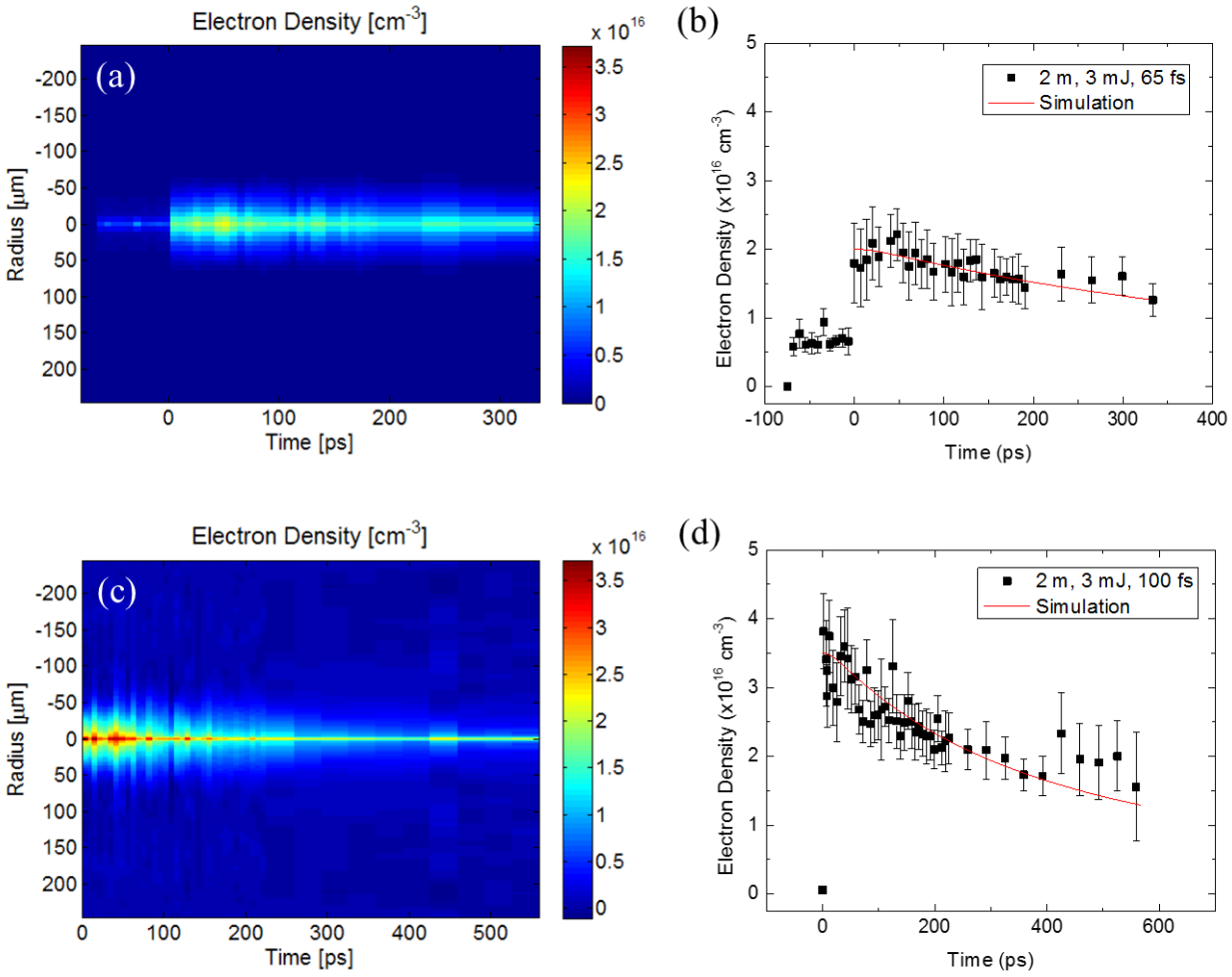

Figure 21: (Left) Plots of the temporal evolution of the radial profile of the electron density at the geometric focus for laser generated plasma produced using an f=2 m lens (E=3 mJ, ω_0=11.9 mm). (Right) Plots of the on-axis electron density for the same conditions as in the plots to the left. The pump beam pulse durations were (a-b) 65 fs and (c-d) 100 fs.

Table 6: Peak electron density and half-life of the laser generated plasma focused by an f=2 m lens (E=3 mJ, ω_0=11.9 mm), for pulse durations of 65 and 100 fs.

Pulse duration (fs)	Focal length (m)	Energy (mJ)	Crossing angle	Peak density (cm^{-3})	Half-life (ps)
65	2.2	2.99±0.074	1.7°	2.0e16	523
100	2.2	3.00±0.031	0.8°	3.5e16	360

3.2 – Kerr Effect

3.2.1 – Varying Energy

The Kerr effect in air was measured for two energy conditions. A focal length of 2 m was employed (NA=5.9×10^{-3}), with a 1.7° angle between pump and probe and a pulse duration of 65 fs. Measurements were made at energies of 3 mJ and 4 mJ (Figure 22). Measurements were taken in increments of 50 fs for a total of 1 ps.

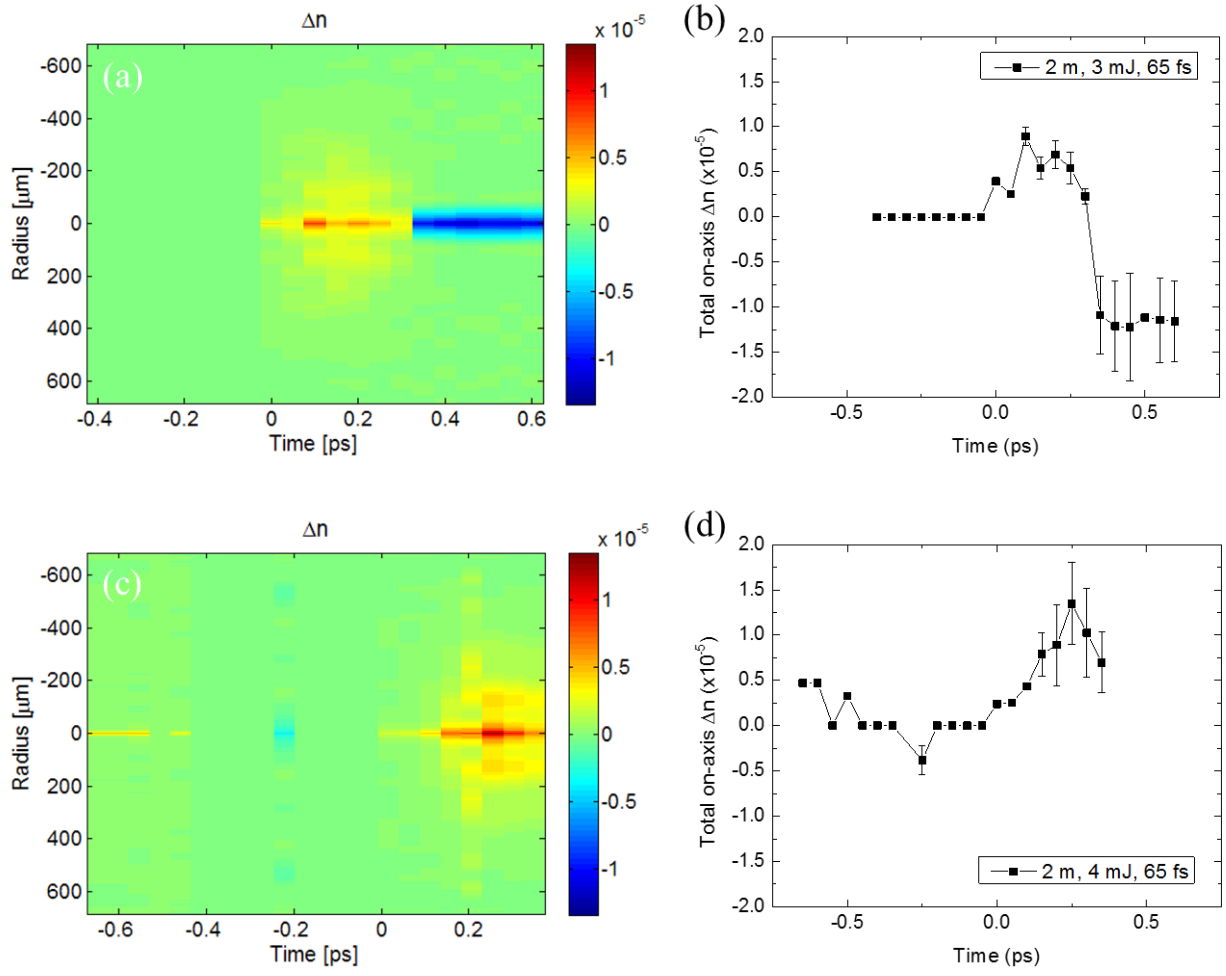

Figure 22: (Left) Plots of the temporal evolution of the refractive index change produced at the geometric focus, by a beam focused with an f=2 m lens (τ=65 fs, ω_0=11.9 mm). (Right) Plots of the total on axis refractive index change induced by filamentation vs. time. Beam conditions are the same as in the plots to the left. The pump beam energies are (a-b) 3 mJ and (c-d) 4 mJ.

3.2.2 –Varying Pulse Duration

Measurements were made of the Kerr effect for different pulse durations. For a 2 m focal length lens (NA=5.9×10^{-3}) and 3 mJ energy, the Kerr effect was observed for pulse durations of 65 fs and 100 fs (Figure 23). Measurements were taken for several delays, for a total time between 0.5 and 1 ps, in increments of ~50 fs.

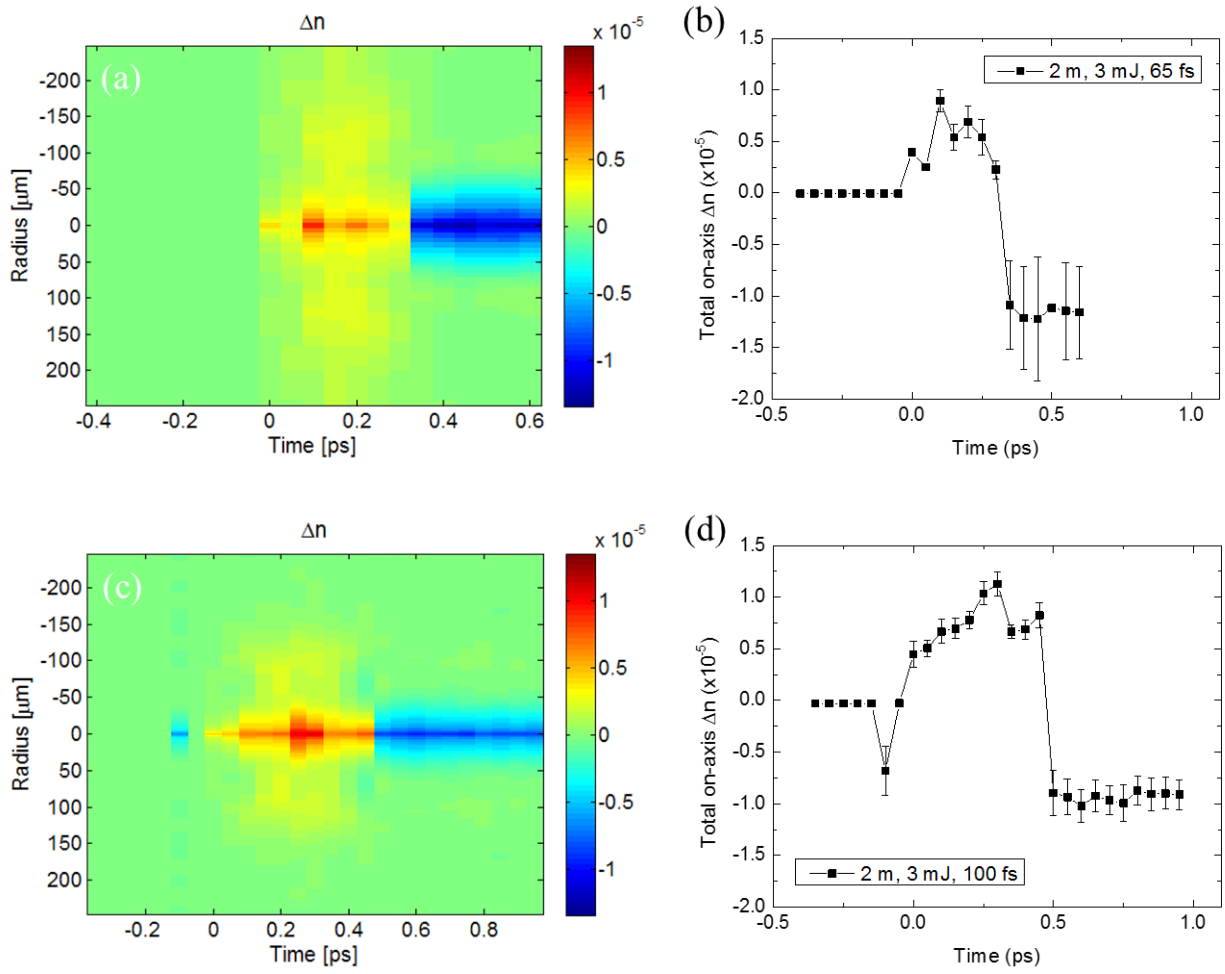

Figure 23: (Left) Plots of the refractive index change induced at the geometric focus by a focused laser beam (f=2 m lens, E=3 mJ, ω_0=11.9 mm). (Right) Plots of the on-axis refractive index change for the same beam conditions as in the plots to the left. The pulse durations are (a-b) 65 fs and (c-d) 100 fs.

3.2.3 – Discussion

In the measurements above, the Kerr effect is not isolated, but rather the total change in refractive index is observed, including the contribution of the plasma. In Figure 22(a), the positive Δn (orange) is caused by the Kerr effect, while the negative Δn (blue) is produced by plasma formation, as in Figure 23. In Figure 22(c), the positive Δn due to the Kerr effect is seen (orange-red), but plasma formation was not captured in this time window. The plots show the full temporal evolution. Initial self-focusing due to the Kerr effect occurs, leading to plasma formation. The plasma continues to grow as the Kerr effect reaches a peak and declines, until Δn reaches zero when the two effects are equal. Then the plasma plays the dominant role and continues long after the pulse, and thus the Kerr effect, are gone.

With this technique, the peak value of the Kerr effect cannot be measured, since it is not secluded from the plasma effect. The same is true for the plasma rise time. In addition, the positive refractive index change displayed in the plots, which should only occur during the pulse, lasts for a significant amount of time (0.25 for τ_p=65 fs and 0.5 ps for τ_p=100 fs) compared to the pulse duration, which is a result of the comparatively low temporal resolution of this measurement technique. However, the measurements were still able to accurately capture the main features of the total refractive index change. The measured peak values agree well with the NLSE simulation displayed in Figure 24(a). Figure 24(b) 'smears' this result out in time to mimic the data taking process, elucidating the overall shape and duration of the measured positive Δn. While in the unaltered simulation, the Kerr effect is more pronounced than the plasma, both experiment and time-averaged simulation show that the peak and minimum values of Δn are equal in magnitude.

The Kerr effect remained relatively constant across all the tested conditions (Figure 22). The simulation (Figure 24) confirms that the Kerr effect produces little to no change in the peak value of Δn for the given conditions. That both the Kerr effect and the plasma densities changed minimally for an NA of 0.0059, under different conditions, agrees well with the fact that this NA falls close to the transition from linear to nonlinear focusing conditions, at which point intensity clamping occurs.

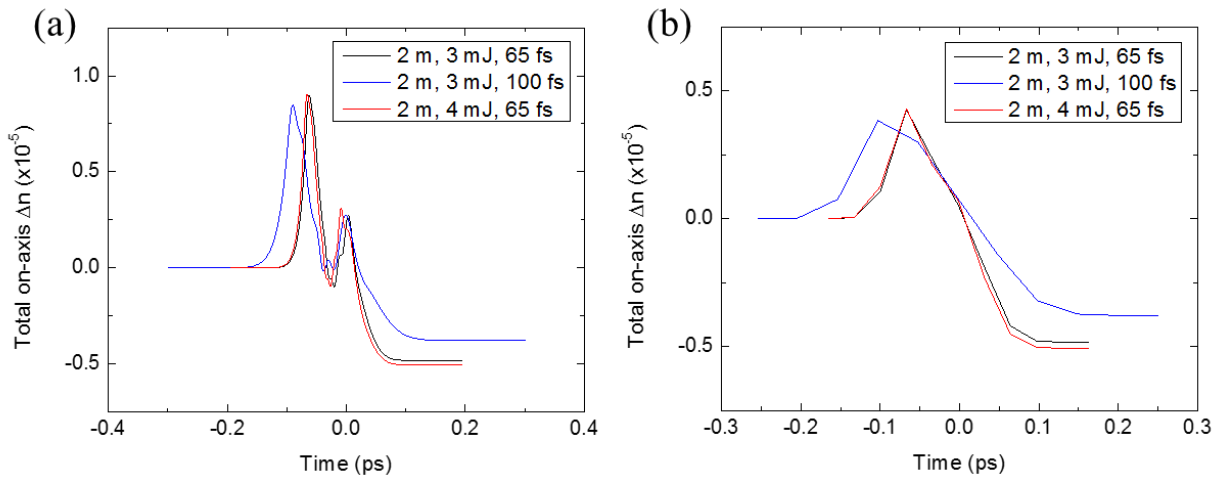

Figure 24: (a) Plots of the total on-axis refractive index change, due to the Kerr effect and plasma generation, simulated using the NLSE code for the conditions in the legend. (b) Plots of the results of the NLSE code averaged in time according to the procedure outlined at the end of section 2.3.3.

3.3 – Full Temporal Profile

Measurements were performed to obtain the full temporal picture of the refractive index change and plasma produced by a laser focused using an f=2 m lens (τ_p=100 fs, E=3 mJ, ω_0=11.9 mm, λ_0=800 nm). The refractive index change due to the Kerr effect and plasma formation are depicted in Figure 25(a) and Figure 26(a). The plasma decay is depicted in Figure 25(b) and Figure 26(b). The corresponding simulations are shown in Figure 27. The experimental total refractive index change reaches a peak at 1.13e-5 and a minimum at -1.02e-5. According to simulation, these

values are 8e-6 and -4e-6 respectively. The on-axis plasma density peaks at 3.5e16 cm^{-3}. The decay simulation shows that the plasma density reaches half of its peak value in 360 ps.

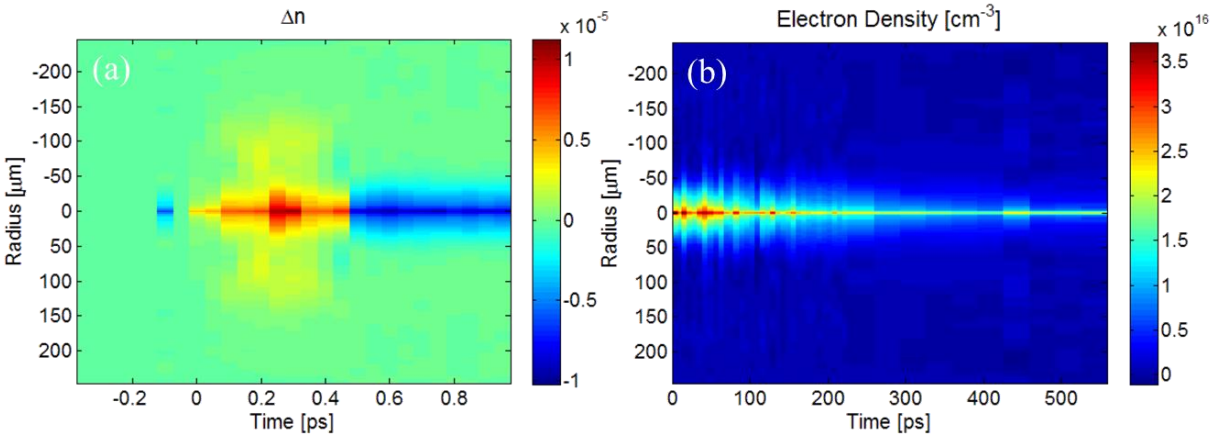

Figure 25: The full temporal profile for a filamenting pulse focused by an f=2 m lens (E=3 mJ, τ=100 fs, ω_0=11.9 mm). (a) The short time scale refractive index modification showing the Kerr effect and plasma formation. (b) The long time scale showing the electron density decay.

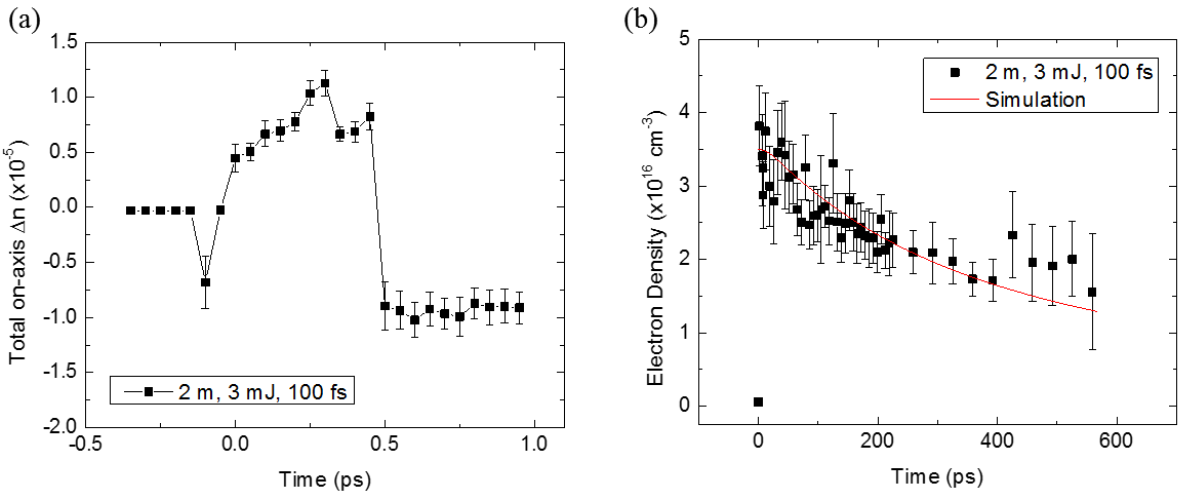

Figure 26: The full temporal profile of a filamenting pulse for the same conditions as in Figure 25. (a) Short time scale showing Δn on-axis. (b) Long time scale showing the on-axis electron density decay.

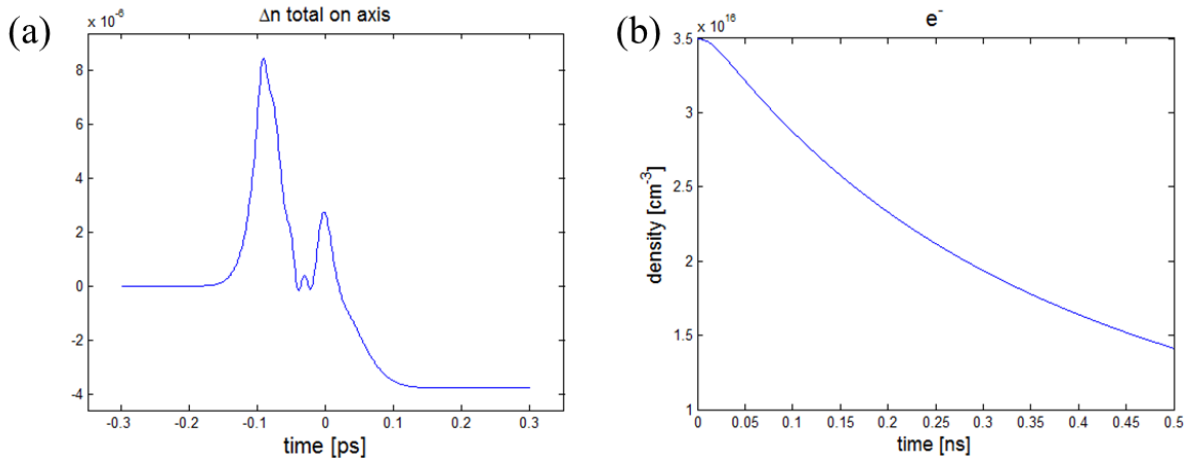

Figure 27: Temporal profile of a filamenting pulse for the same conditions as in Figure 25, accounting for the angle correction factor of 0.012. (a) Simulation of the on-axis refractive index change due to the Kerr effect and plasma, using the NLSE code. (b) Simulation of the electron density decay.

CHAPTER 4 – CONCLUSION

The filament induced refractive index modification in air has been studied, contributing to the fundamental understanding of filament formation and propagation. Many applications make use of the refractive index modifying properties of a filament, and these observations further improve the understanding required to bring these applications to fruition. The results in this thesis can aid in the design of filament arrays as wave guides or in the use of filaments for guiding electric discharge.

As this thesis has shown, the interferometric technique enables measurement of very low plasma densities compared to other techniques, such as the acoustic method. The only other experimental scheme that enables similar sensitivity is holography. While measuring THz scattering is still the most sensitive method, interferometry also retrieves spatial information about the filament cross-section. However, a tradeoff exists between sensitivity and axial spatial resolution, which is truly the downfall of this method. Increasing the interaction length by decreasing the crossing angle degrades the spatial resolution along filament propagation and the temporal resolution.

The electron density was measured for several conditions. The results confirm that the plasma density is not clamped in the linear focusing regime. The peak density decreases to half its value in a shorter amount of time for higher energy, NA and pulse duration. The data showed an increase in plasma density with increasing energy, numerical aperture, and pulse duration. However, the peak electron density changed little for the various conditions when considering an NA of 5.9×10^{-3}, which is near to the transition point between linear and nonlinear focusing

regimes. The model, accounting for three-body and two-body dissociative recombination with O_2^+ and formation of complex ions, agreed well with the experimental results.

The Kerr effect was measured under different initial conditions, with an NA of 5.9×10^{-3}. Experiment showed little to no change in the magnitude of the Kerr effect for different energies or pulse durations. Changes in initial parameters produced little to no effect as the NA approached NA_T. The peak values agreed well with the NLSE code results. The time-averaged simulations reflected the overall shape and extended duration of the experimental results.

The interferometric technique is able to capture the temporal evolution of the filament from initial self-focusing to plasma formation and decay. However the effects of plasma and Kerr cannot be isolated, so the plasma rise time and peak Kerr effect are lost in the total refractive index modification. While unable to resolve the finer features of the total Δn due to the insufficient temporal resolution, this technique can accurately and directly measure the total refractive index modification, as well as the peak plasma density and plasma decay.

Though the fundamental properties of a filament are well known, they are highly influenced by different physical parameters. The work presented in this thesis explored the impact of different initial conditions on the Kerr effect and plasma in the linear regime of filamentation. These studies contribute to the overall understanding of filamentation and further the progress towards real-world applications.

REFERENCES

[1] A. Couairon and A. Mysyrowicz, "Femtosecond Filamentation in Transparent Media," *Physics Reports,* vol. 441, pp. 47-189, 2007.

[2] E. Dawes and J. Marburger, "Computer Studies of Self-Focusing," *Physical Review,* vol. 179, pp. 862-868, 1969.

[3] Z. Deng and H. Eberly, "Multiphoton absorption above ionization threshold by atoms in strong laser fields," *Journal of the Optical Society of American B,* vol. 2, pp. 486-493, 1985.

[4] M. Mlejnek, E. Wright, and J. Moloney, "Dynamic spatial replenishment of femtosecond pulses propagating in air," *Optics Letters,* vol. 23, pp. 382-384, 1998.

[5] A. Braun, G. Korn, X. Liu, D. Du, J. Squier, and G. Mourou, "Self-channeling of high-peak-power femtosecond laser pulses in air," *Optics Letters,* vol. 20, pp. 73-75, 1995.

[6] C. D'Amico, A. Houard, M. Franco, B. Prade, and A. Mysyrowicz, "Conical Forward THz Emission from Femtosecond-Laser-Beam Filamenation in Air," *Physical Review Letters,* vol. 98, p. 4, 2007.

[7] J. Kasparian, R. Ackermann, Y.-B. Andre, G. Mechain, G. Mejean, B. Prade, *et al.*, "Electric events synchronized with laser filaments in thunderclouds," *Optics Express,* vol. 16, pp. 5757-5763, 2008.

[8] T.-J. Wang, Y. Wei, Y. Liu, N. Chen, Y. Liu, J. Ju, *et al.*, "Direct observation of laser guided corona discharges," *Scientific Reports,* vol. 5, pp. 1-5, 2015.

[9] S. L. Chin, T.-J. Wang, C. Mareau, J. Wu, J. Liu, O. Kosareva, *et al.*, "Advances in Intense Femtosecond Laser Filamentation in Air," *Laser Phsyics,* vol. 22, pp. 1-53, 2011.

[10] Y. Ren, M. Alshershby, and Z. Hao, "Microwave guiding along double femtosecond filaments in air," *Physical REview E,* vol. 88, 2013.

[11] A. Dormidonov, V. Valuev, V. Dimitriev, S. Shlenov, and V. Kandidov, "Laser Filament Induced Microwave Waveguide in Air," in *International Conference on Laser, Applications, and Technologies,* 2007, pp. 1-6.

[12] J. Ju, J. Liu, H. Liang, Y. Chen, H. sUn, Y. Liu, *et al.*, "Femtosecond laser filament induced condensation and precipitation in a cloud chamber," *Scientific Reports,* vol. 6, pp. 1-10, 2016.

[13] S. Chin, H. Xu, Q. Luo, F. Theberge, W. Liu, J. Daigle, *et al.*, "Filamentation "remote" sensing of chemical and biological agents/pollutants using only one femtosecond laser source," *Applied Physics B,* vol. 95, pp. 1-12, 2009.

[14] H. Ladouceur, A. Baronavski, D. Lohrmann, P. Grounds, and P. Girardi, "Electrical conductivity of a femtosecond laser generated plasma channel in air," *Optics Communications,* vol. 189, pp. 107-111, 2001.

[15] N. Vujičić, H. Skenderovic, T. Ban, D. Aumiler, and G. Pichler, "Low density plasma channels generated by femtosecond pulses," *Applied Physics B,* vol. 82, pp. 377-382, 2006.

[16] T. Petrova, H. Ladouceur, and A. Baronavski, "Nonequilibrium dynamics of laser-generated plasma channels," *Physics of Plasmas* vol. 15, 2008.

[17] D. Abdollahpour, S. Suntsov, D. Papazoglour, and S. Tzortzakis, "Measuring easily electron plasma densities in gases produced by ultrashort lasers and filaments," *Optics Express,* vol. 19, pp. 16866-16871, 2011.

[18] M. Alshershby, Y. Ren, J. Qin, Z. Hao, and J. Lin, "Diagnosis of femtosecond plasma filament by channeling microwaves along the filament," *Applied Physics Letters,* vol. 102, 2013.

[19] S. Bodrov, N. Aleksandrov, M. Tsarev, A. Murzanev, I. Kochetov, and A. Stepanov, "Effect of an electric field on air filament decay at the trail of an intense femtosecond laser pulse," *Physical Review E,* vol. 87, 2013.

[20] A. Ionin, S. Kudryashov, D. Mokrousova, L. Seleznev, D. Sinitsyn, and E. Sunchugasheva, "Plasma channels under filamentation of infrared and ultraviolet double femtosecond laser pulses," *Laser Physics Letters,* vol. 11, p. 4, 2014.

[21] A. Ionin, L. Seleznev, and E. Sunchugasheva, "Formation of plasma channels in air under filamentation of focused ultrashort laser pulses," *Laser Physics Letters,* vol. 25, p. 14, 2015.

[22] H. Zuo-Qiang, Y. Jin, Z. Jie, L. Yu-Tong, Y. Xiao-Hui, Z. Zhi-Yuan, *et al.*, "Acoustic diagnostics of plasma channels induced by intense femtosecond laser pulses in air," *Chinese Physical Letters,* vol. 22, pp. 636-639, 2005.

[23] J. Papeer, M. Botton, D. Gordon, P. Sprangle, A. Zigler, and Z. Henis, "Extended lifetime of high density plasma filament generated by a dual femtosecond-nanosecond laser pulse in air," *New Journal of Physics,* vol. 16, 2014.

[24] J. Papeer, D. Gordon, P. Sprangle, M. Botton, and A. Zigler, "Temporal evolution of femtosecond laser induced plasma filament in air and N2," *Applied Physics Letters,* vol. 103, 2013.

[25] J. Bernhardt, W. Liu, F. Theberge, H. Xu, J. Daigle, M. Chateauneuf, *et al.*, "Spectroscopic analysis of femtosecond laser plasma filament in air," *Optics Communications,* vol. 281, pp. 1268-1274, 2008.

[26] S. Bodrov, V. Bukin, M. Tsarev, A. Murzanev, S. Garnov, N. Aleksandrov, *et al.*, "Plasma filament investigation by transverse optical interferometry and terahertz scattering," *Optics Express,* vol. 19, pp. 6829-6835, 2013.

[27] F. Théberge, W. Liu, P. Simard, A. Becker, and S. Chin, "Plasma density inside a femtosecond laser filament in air: Strong dependence on external focusing," *Phsyical Review E,* vol. 74, 2006.

[28] Z. Sun, J. Chen, and W. Rudolph, "Determination of the transient electron temperature in a femtosecond-laser-induced air plasma filament," *Physical Review E,* vol. 83, 2011.

[29] J. Liu, Z. Duan, Z. Seng, X. Sie, Y. Deng, R. Li, *et al.*, "Time-resolved investigation of low-density plasma channels produced by a kilohertz femtosecond laser in air," *Physical Review E,* vol. 72, 2005.

[30] G. Rodriguez, A. Alenzuela, B. Yellampalle, M. Schmitt, and K.-Y. Kim, "In-line holographic imaging and electron density extraction of ultrafast ionized air filaments," *Journal of the Optical Society of America,* vol. 25, pp. 1988-1997, 2008.

[31] M. Durand, A. Jarnac, Y. Liu, B. Prade, A. Houard, V. Tikhonchuk, *et al.*, "Dynamics of plasma gratings in atomic and molecular gases," *Physical Review E,* vol. 86, 2012.

[32] D. Papazoglou and S. Tzortzakis, "In-line holography for the characterization of ultrafast laser filamnetation in transparent media," *Applied Physics Letters,* vol. 93, 2008.

[33] Y.-H. Chen, S. Varma, T. Antonsen, and H. Milchberg, "Direct measurement of the electron density of extended femtosecond laser pulse-induced filaments," *Physical Review Letters,* vol. 105, 2010.

[34] J. Wahlstrand, Y.-H. Chen, Y.-H. Cheng, S. Varma, and H. Milchberg, "Measurements of the high field optical nonlinearity and electron density in gases: application to filamentation experiments," *IEEE Journal of Quantum Electronics,* vol. 48, 2012.

[35] M. Centurion, Y. Pu, and D. Psaltis, "Holographic capture of femtosecond pulse propagation," *Journal of Applied Physics,* vol. 100, 2006.

[36] T. Balciunas, A. Melninkaitis, G. Tamosauskas, and V. Sirutkaitis, "Time-resolved off-axis digital holography for characterization of ultrafast phenomena in water," *Optics Letters,* vol. 33, pp. 58-60, 2008.

[37] T. Balciunas, A. Melninkaitis, A. Vanagas, and V. Sirutkaitis, "Tilted-pulse time-resolved off-axis digital holography," *Optics Letters,* vol. 341, pp. 2715-2717, 2009.

[38] N. Siaulys, A. Melninkaitis, and A. Dubietis, "In situ study of two interacting femtosecond filaments in sapphire," *Optics Letters,* vol. 40, pp. 2285-2288, 2015.

[39] K. Lim, "Laser Filamentation - Beyond Self-focusing and Plasma Defocusing," PhD, College of Optics and Photonics, University of Central Florida, Orlando, Florida, 2014.

[40] M. Takeda, "Fourier-Transform Method of Fringe-Pattern Analysis for Computer-Based Topography and Interferometry," *Journal of the Optical Society of America,* vol. 72, 1982.

[41] F. Harris, "On the use of windows for ahrmonic analysis with the discrete Fourier transform," *Proceedings fo the IEEE,* vol. 66, pp. 51-83, 1978.

[42] S. Ma, H. Gao, and L. Wu, "Modified Fourier-Hankel Method Based on Analysis of Errors in Abel Inversion Using Fourier Transform Techniques," *Applied Optics,* vol. 47, 2008.

[43] W. C. Kreye, J. W. Hemsky, and M. L. Andrews, "A simple numerical method for a modified Abel inversion in which the density can eb approximated by elliptical symmetry," *Journal of Physics D: Applied Physics,* vol. 26, pp. 1836-1842, 1993.

[44] E. Anokhin, M. Popov, I. Kochetov, N. Aleksandrov, and A. Starikovskii, "Plasma Decay in High-Voltage Nanosecond Discharges in Oxygen-Containing Mixtures," *Plasma Physics Reports,* vol. 42, pp. 59-67, 2015.